#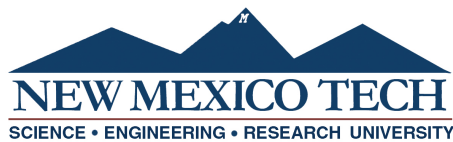 SENSITIVITY OF PARTICLE FLUXES MEASURED BY THE VAN ALLEN PROBES TO VARIATIONS IN THE MODELED MAGNETIC AND ELECTRIC FIELDS

by

John Chilleri

New Mexico Institute of Mining and Technology
Socorro, New Mexico
December 12, 2020

This thesis is dedicated to my family. My entire life has been blessed with overflowing support and encouragement from my loved ones.
Thank you mom, dad, and brothers!

John Chilleri
New Mexico Institute of Mining and Technology
December 12, 2020

ACKNOWLEDGMENTS

I would like to thank Dr. Brian Borchers and Dr. Anders Jorgensen for their huge time commitment, as well as the invaluable guidance and feedback they provided throughout the project. I would also like to thank Dr. Oleg Makhnin who served on my committee.

This thesis was typeset with LaTeX[1] by the author.

---

[1]The LaTeX document preparation system was developed by Leslie Lamport as a special version of Donald Knuth's TeX program for computer typesetting. TeX is a trademark of the American Mathematical Society. The LaTeX macro package for the New Mexico Institute of Mining and Technology thesis format was written by John W. Shipman.

ABSTRACT

The Earth's magnetic field extends into space resembling a dipole, where it interacts with the solar wind produced by the Sun. The interaction stretches, compresses, and alters the shape of the magnetic field. Simultaneously, there exist charged particles traveling through space, which are affected by the magnetic and electric fields of Earth, that are occasionally trapped in Earth's magnetosphere. The Van Allen Probes are two satellites that study the Van Allen radiation belts around Earth; regions populated with charged particles. We propose that the observed particle fluxes at the two satellites may reveal information about the magnetic and electric fields. In order to test this, we employ the International Geomagnetic Reference Field and Tsyganenko magnetic field models. An electric field model is obtained by using the magnetic field models in conjunction with the Sojka model. These models include a parameter K_p, a value that captures the global magnetic activity. We simulate particles along their guiding centers through space to compare satellite observations of particle fluxes with modeled particle fluxes.

The models are tested with various K_p values to ascertain the model sensitivity to changes in this index, as well as to identify which K_p value best matches the observational data. In order to validate the method, two days, one of low and one of medium observed K_p, were selected for simulation. Varying the model's K_p indices incurs observable change with respect to the electric field. The resulting modeled spectra are also reasonably consistent with the data. The best matching spectrum was produced from the model with K_p equivalent to the observed K_p in the low-K_p day. The optimal K_p is less discernible for the medium-K_p day. The simulation results are not yet sufficient to fully resolve K_p but do suggest future data and modeling approaches for further study.

Keywords: GUIDING CENTER APPROXIMATION; SPACE PHYSICS; RADIATION BELTS; SPACE WEATHER

CONTENTS

LIST OF TABLES

LIST OF FIGURES

This thesis is accepted on behalf of the faculty of the Institute by the following committee:

Brian Borchers

———————————————————————————————

Academic and Research Advisor

Anders Jorgensen

———————————————————————————————

Oleg Makhnin

———————————————————————————————

I release this document to the New Mexico Institute of Mining and Technology.

John Chilleri   November 20, 2020

———————————————————————————————

CHAPTER 1

INTRODUCTION

1.1   Background

A magnetosphere is the region of space surrounding a magnetized planet or other space object in which charged particles are affected by that object's magnetic field ([10],[14]). Often times the magnetic field resembles a dipole near the surface of the planet, for which analytic solutions using L-shells exist. This definition of L-shell is a parameter describing the set of magnetic field lines that intersect the magnetic equator at L Earth radii ([8], [21]). The more distant field lines, however, can be greatly influenced by external factors. The Earth's magnetic field is one such example, with a compressed magnetic field on the dayside, that is, the side facing towards the Sun, and a stretched magnetic field on the night-side, the side facing away from the Sun. These distortions in the magnetic field are in large part due to the interaction with the solar wind. The solar wind is a supersonic outward flow of ionized gases and magnetic fields from the sun. Variations in the solar wind speed can produce changes or distortions in the Earth's magnetosphere, for example, the initiation of magnetic storms ([8], [21]). Global changes in the magnetic field can be quantified by the K_p-index, where K stands for the German word Kennziffer meaning "characteristic digit", and the subscript p stands for "planetary". The K_p-index ranges from zero to nine, with small values such as one indicating low activity, and large values, beginning with five, indicating high activity; often a geomagnetic storm [20]. The effects of these storms on the magnetic field can be dramatic, stretching a nearby field line on the night-side tens of Earth radii away from its dipolar location. Accordingly, magnetic field models have been created which parameterize these changes in the magnetic field in terms of the K_p index.

Moving in accordance with the magnetic and electric fields are populations of charged particles. The magnetic and electric fields conduct the particles along intricate paths, causing the particles to undergo small gyratory motion and orbital drift (see Figure 1.1). The force produced by the magnetic and electric fields acting on the particles is described by the Lorentz force equation ([8], [21]). The

1

magnitude and direction of this force are dependent on the kinetic energy and pitch angle of the particle. The pitch angle of a particle is the angle between the particle's velocity vector and the local magnetic field ([8], [21]). A particle with zero pitch angle has a velocity vector parallel to the local magnetic field. A particle with 90 degree pitch angle is said to be mirroring. A particle mirrors when it decelerates and reverses direction due to the forces it experiences as it approaches a region of stronger magnetic field, this concept is discussed in more detail in Chapter 3 [3]. Magnetic mirroring forces cause the trapping of energetic charged particles in the dipole-like field lines near Earth. Part of this particle population is referred to as the Van Allen radiation belts [4].
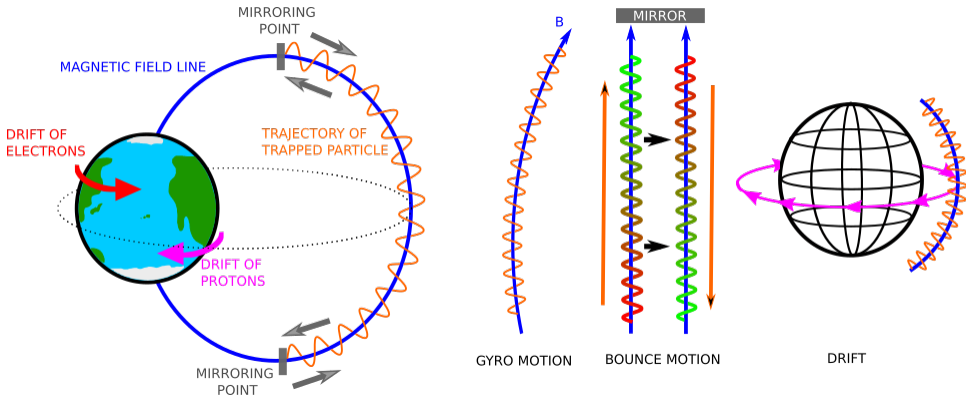
Figure 1.1: Particle motion in the magnetosphere. Inspired by [16].

Launched on August 30, 2012, the Van Allen Probes (formerly Radiation Belt Storm Probes, RBSP) are two satellites that study the Van Allen radiation belts around Earth [5]. The two satellites follow roughly the same nine hour orbit but with a delay of a few hours. The Van Allen Probes are equipped with a comprehensive suite of instrumentation for measuring species, energy, and pitch angle of charged particles. The data produced by these satellites are freely available and include orbit locations, spectrograms, K_p indices, and other information recorded since the commissioning of the satellites in 2012 [6]. In this work we have used data from the HOPE (Helium, Oxygen, Proton, and Electron) instrument.

1.2 Statement of the Problem

One of the National Aeronautics and Space Agency's (NASA) four general scientific objectives for the Van Allen Probes Mission is to "Understand how the radiation belts change in the context of geomagnetic storms" [5]. Aligned with

this objective, this thesis constructs a model for tracing particles in Earth's magnetosphere, which in conjunction with satellite data, will be used to examine the extent to which the magnetic field can be constrained by multi-point particle observations. Specifically, we determine the extent to which the K_p parameter, as a proxy for electric and magnetic fields, can be determined.

1.3 Purpose and Significance

This thesis introduces a method for estimating the Earth's magnetic activity index, K_p, as a proxy for the magnetic and electric fields from satellite data and particle tracing simulations. The results of the method will contain information regarding the accuracy of the models, as well as implicate to some extent the changes in the magnetic field with respect to changing activity levels. Consequentially, the significance of this thesis aligns with the goals of the Van Allen Probes mission. Furthermore, understanding the radiation belt environment and its variability has important practical applications in the areas of spacecraft operations, spacecraft system design, mission planning, and astronaut safety [5].

1.4 Assumptions, Limitations, and Scope

These models are operated under the assumption that the magnetic field is time-stationary. The magnetic and electric fields of Earth change with the tilt angle of Earth's magnetic axis. Although this is accounted for in the Tsyganenko and IGRF models, we use the models at a fixed time for simplicity. It should be noted that a dynamic value for time would be incredibly computationally expensive. The justification is that the simulations will not proceed through enough real-time for Earth's magnetic axis to have significantly rotated. This is supplemented by starting at a trailing satellite and integrating to the leading satellite, in which the difference in time of measurement at the starting and ending locations is restricted to a small time interval of less than 9 hours. Additionally, the fixed date and time that is selected corresponds to a period of observed, unchanging K_p, which implies that little change is occurring in the magnetic field.

We also assume that both electric potential and flux are constant along magnetic field lines. The assumption of constant electric potential is because the charged particles move freely along magnetic field lines, hence any field-aligned potential difference is quickly canceled by particle motion. The assumption of

constant flux along magnetic field lines derives from the idea that there are equivalent populations of identical particles distributed up and down magnetic field lines; the simulations we perform model one representative particle. Assuming electric potential is constant along field lines, we will employ models of the electric potential on the Earth's surface to estimate the electric field. These models integrate back to Earth's surface where they compute the potential.

Otherwise, usage of the models is limited by the computational requirements. Whilst adaptations were made to increase efficiency at the cost of accuracy, the run-time is still sufficiently large to prevent extensive simulation, even with the exceptional computer resources available. To be specific, simulations are performed on a cluster of ten blades with twelve cores each.

Finally, this thesis is concerned with the primary contributors to particle motion; the magnetic and electric fields. There are additional, outside forces that may have small impacts, such as iron artifacts on Earth [2], but they are out of the scope of consideration.

1.5   Research Design

This thesis considers particles with varying pitch angles, energies, and initial positions. The pitch angles will vary over eleven values, matching the resolution of the observed data. The energies and locations will be selected around distinct features of the observed spectrograms, which intuitively are subject to change between K_p indices. That is, distinct features are easily identifiable, while it's difficult to observe change inside regions of constant or similar flux. Additionally, features covering all observed energies will be selected to observe the particle motion under dominant contribution from both components, meaning the electric field $\mathbf{E}$ and magnetic field $\mathbf{B}$, of the Lorentz force (the Lorentz force is discussed in detail in Chapter 2),

$$\mathbf{F} = q\mathbf{E} + q\mathbf{v} \times \mathbf{B} \tag{1.1}$$

that is, the $\mathbf{E}$ and $\mathbf{v} \times \mathbf{B}$ components, in addition to observing motion dictated by both components equally. The $\mathbf{E}$ component dominates at lower energies, which simulation data suggests is below a few keV, while the $\mathbf{v} \times \mathbf{B}$ term dominates at higher energies. In order to capture major contribution by the magnetic and electric fields, we selectively use the HOPE satellite data, which has an energy range between zero eV and 52 keV. The initial positions will be selected to be coincident with orbital locations of the satellites; our intention is to trace particles in order to obtain connections between the trailing and leading satellite, at which points

the observational data measured by both satellites is expected to be comparable (Figure 1.2).
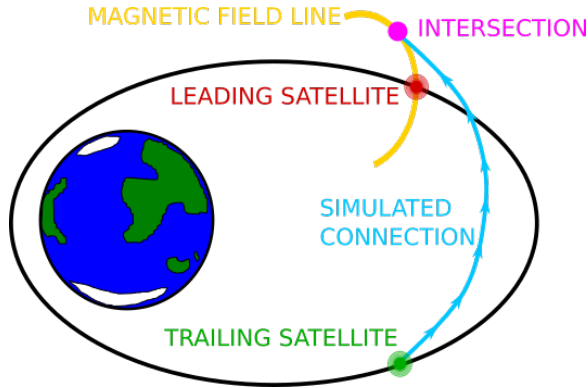
Figure 1.2: Simulated connections between trailing and leading satellite.

In order to trace particles in Earth's magnetosphere, we use parameterized models of the magnetic and electric fields. Models of varying accuracy and complexity exist to approximate the magnetic and electric fields surrounding Earth. Regarding these fields, three sets of models are considered. The first set of models use a dipole approximation of both fields in conjunction with the Sojka model [18] of electric potentials at the Earth's surface. Referred to as the full gyration model, this employs the aforementioned field models to obtain the necessary field vectors for use in the Lorentz force calculation, which drives the particle motion. The resultant path of the particle should display all expected motions: small gyration, orbital drift, and mirroring. However, the full gyration model is both inaccurate and inefficient, as the dipole model is overly simplistic, and integrating along small gyrations is computationally infeasible for an eventual large number of simulations.

Consequentially, the second model, aimed at improving efficiency, maintains the use of the dipole approximations, but traces the guiding center of the particle rather than the particle itself. The guiding center is essentially the line about which the particle spirals (the guiding center is discussed in greater detail in Chapter 3) [11]. By tracing the guiding center rather than the gyrating particle, the integration becomes much simpler and the model is many times faster, with little error introduced.

The third superlative model aims to accurately reproduce particle motion by utilizing advanced models of the magnetic field, which in turn redefines the tracing in computation of the electric field. The magnetic field will be modeled by the standard International Geomagnetic Reference Field (IGRF) [22] in combination with a Tsyganenko model (T89c) [23]. The electric field will be modeled by

the interaction between the advanced magnetic field and the Sojka model for the surface potential. The overall model contains adjustable parameters, such as the K_p magnetospheric activity index for both the electric and magnetic fields. Although physically there is only one K_p, the K_p input to the magnetic and electric fields are treated as different parameters in our experiments.

Using the third model, particles can be traced through the magnetosphere, provided an initial pitch angle, energy, and position. By spawning an ensemble of particle populations along the orbital path of the trailing satellite (along features in the spectrogram), and tracing them to an intersection later in the leading satellite's orbit, predicted and observed pairs of flux values can be obtained. Inherently, such an intersection is improbable; however, as these particles are representatives of a stream of identical particles, an intersection occurs if the simulated particle crosses any magnetic field line which also crosses the satellite orbit, which can then be mapped back to the satellite's exact location at the corresponding point in the orbit. This works assuming flux is constant along magnetic field lines, so by mapping it back to the satellite's location, the flux prediction or estimate should remain the same. Ideally a full spectrogram could be reconstructed, but such a task would require an immense amount of computation. The K_p parameter allows for the adjustment of the magnetic field in a crude way to test which geometry, of the ones that can be created with the single parameters, best matches the particle fluxes. This allows for flux pairs to be formed for varying magnetospheric activity levels. These pairings will be analyzed against Van Allen Probe data to determine if inverse estimation of the K_p parameter is possible.

CHAPTER 2

DATA QUALITY AND CAVEATS

Before proceeding to the modeling and results sections of this thesis, the quality of the data must be addressed upfront. In particular, the satellite data is difficult to statistically analyze, due to the low count regime in which it operates, alongside a lack of information regarding conversion factors. Both of these will be expanded upon in the upcoming sections.

2.1 Satellite Particle Counts

According to the HOPE project website, one data caveat is that the HOPE satellite data (which is the instrument of interest in this thesis) operates in a low count regime [19]. A majority of the fluxes are computed from a measurement of fewer than ten particle counts. Furthermore, if no particles are observed, that is, a count of zero, then the flux of such particles in that region is estimated to be zero. This is additionally complicated by an undocumented conversion factor that produces fluxes of multiple orders of magnitude from singular counts. Therefore, normal Chi-squared statistics cannot be applied to this data given the low counts underneath the flux values. Beyond this, Poisson statistics are also infeasible due to the undocumented counts to flux conversion factor. When contacted regarding this conversion, the scientists in charge of the data explained that the conversion factor is based off energy, time, as well as other variables [15]. This time dependence is highly variable, changing on the order of seconds.

2.2 Satellite Data Visualization

In order to fully understand the data and the logic behind some approaches taken in this thesis, some depictions of the flux data are presented. First consider

the standard, spin-averaged spectrogram for one orbit. Note that this spectrogram is roughly representative of all spectrograms for all days and times.
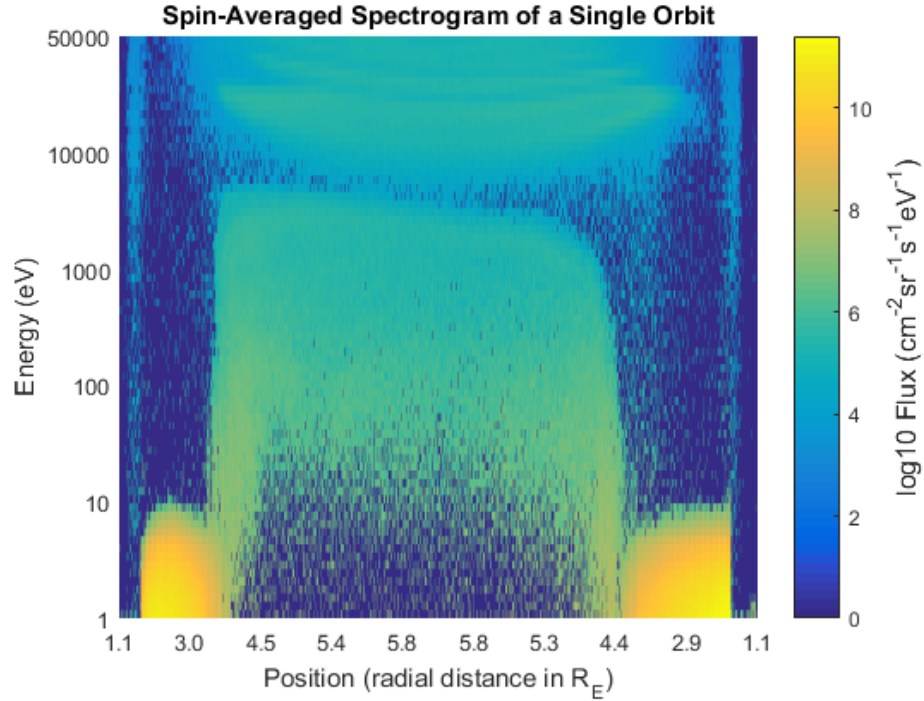
Figure 2.1: Spin-averaged spectrogram of a single orbit. Note that the left and right sides of the spectrogram correspond to the day-side orbit, while the center of the spectrogram corresponds to the night-side, more distant orbit.

The dark blue corresponds to flux values of zero (one was added before taking the log). Notice how there is a scattering of zero fluxes amongst these regions of otherwise $10^5\ cm^{-2}sr^{-1}s^{-1}eV^{-1}$ flux. This is the variability in flux due to the difference between zero and one counts. Furthermore, this spectrogram is spin-averaged while the thesis considers pitch angles individually. Consequently, the actual data used in simulation has a lower signal-to-noise ratio (SNR). For example, consider the two following spectrograms: the first is the spectrogram corresponding to a pitch angle of 90 degrees, the second corresponds to a pitch angle of 4.5 degrees.
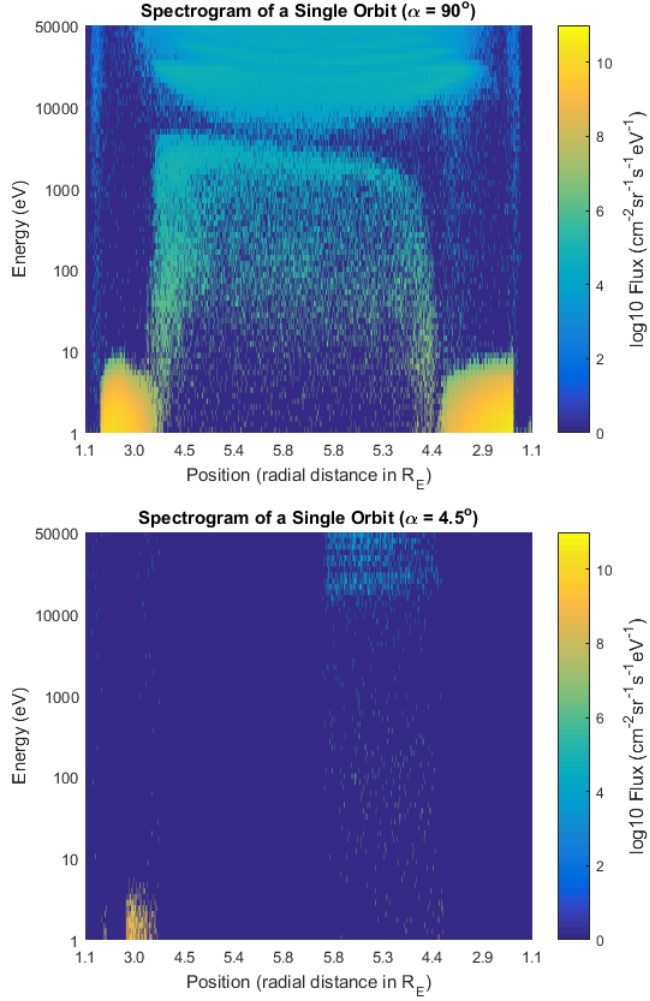
Figure 2.2: Spectrograms of a single orbit for pitch angles $\alpha = 90°$ and $\alpha = 4.5°$, respectively.

We consider 11 pitch angles spaced between 0 and 180 degrees. The most field-aligned pitch angles (4.5 and 175.5 degrees) have less useful data, while the pitch angles closer to 90 degrees typically yield higher SNR data. Even in the case of $\alpha = 90°$, one can still see far more zero fluxes, as opposed to the spin-averaged spectrogram. Otherwise, there are regions that maintain themselves better across the individual pitch angles. Namely the yellow, high-flux regions at the lower sides (plasmasphere), and the medium flux area at the upper middle. As it turns out, the high-flux yellow regions in the plasmasphere do not provide much insight as to the underlying K_p parameter. This is likely because these occur at radially close positions on the day-side of Earth, where the dipole-like

9

field is dominant. Similarly, the upper region does not have obvious, rigidly defined features that would be expected to shift, thus it does not greatly assist in identifying the K_p.

2.3 Basic Statistics of the Satellite Data

Over 75% of the flux values measured by the satellite are either invalid or zero: roughly 65% zero, 10% invalid from one sample day. In an attempt to justify the assigned flux values, which are computed from counts, one can delve into the counts data. Although it was mentioned before, it is worth reiterating the following information before proceeding to the next chapter. According to the Data Quality and Caveats, HOPE satellite data experiences "Frequent periods when counting rates are near 1-count level. When the fluxes are low, counting statistics can produce significant errors and uncertainties" [19]. Furthermore, the method by which counts are converted to fluxes has not been disclosed at this time, but has been revealed to be a function of at least time, position, pitch angle, and energy [15]. The only known conversion is that zero count equates to zero flux, which leads to the high proportion of zeros. In the data there are small count observations converted to huge flux estimates neighboring zero count observations converted to zero flux estimates. Thus the data must be approached with caution. In an attempt to overcome these local disparities, the spectrograms were smoothed with different kernels, optimized for each simulation; this idea will be expanded on later. One such smoothed spectrogram is shown in Figure 2.3.
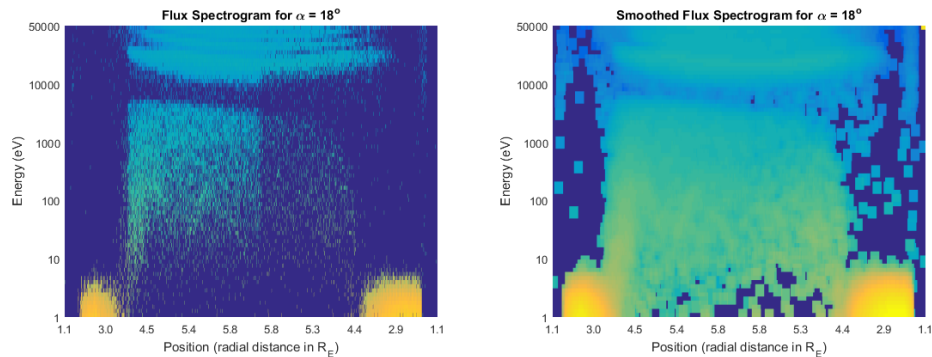
Figure 2.3: Example of a spectrogram with and without smoothing.

Note that the smoothing occurs on each spectrogram for each pitch angle. Figure 2.3 shows a spin-averaged spectrogram with its smoothed version.

CHAPTER 3

EQUATION DEVELOPMENT AND IMPLEMENTATION

3.1 Full Gyration Model

There are numerous forces acting on particles in the magnetosphere of Earth. Four such characteristics of particle motion will be considered:

(1) The first is the general orbital motion. Charged particles move along the magnetic field lines of Earth, resulting in an orbit of Earth ([8], [21]). These particles are confined to this precise orbit by stabilizing forces produced by the magnetic field.

(2) The second characteristic is the gyratory motion caused by the Lorentz force. If a particle of charge q moves through a magnetic field $\mathbf{B}$ and an electric field $\mathbf{E}$ with velocity $\mathbf{v}$, it experiences a force known as the Lorentz force,

$$\mathbf{F} = q\mathbf{E} + q\mathbf{v} \times \mathbf{B}, \tag{3.1}$$

This force causes the charged particle to undergo a gyratory motion ([8], [21]).

(3) The third characteristic is the mirroring of particles along their magnetic field paths. A charged particle moving within a region of magnetic field experiences a Lorentz force that causes it to move in a helical (corkscrew) path along a magnetic field line. The radius of the circle that the particle path sweeps out is called the radius of gyration or gyroradius. If it enters a region of denser magnetic field lines, a field gradient, the combination of the radial component of the fields and the azimuthal motion of the particle results in a force pointed against the gradient, in the direction of the lower magnetic field. It is this force that can reflect the particle, causing it to decelerate and reverse direction ([8], [21]).

(4) The final characteristic is the effects of the magnetic and electric fields by their interaction with the charged particles, which determines the direction of the motion/orbit.

The full gyration model guides a charged particle in accordance with modeled magnetic and electric fields using the Lorentz force. This equation (3.1) naturally accounts for each of the above characteristics, given particle charge and separately computed magnetic and electric fields.

The charge is known based on which particle is considered (electron or proton), and both the magnetic and electric field vectors will be computed using existing models. The 3D velocity and the 3D position together compose the state vector in the integration. In order to integrate over the velocity vector, an acceleration vector (the derivative of the velocity vector) must be calculated at each step. Integrating over position requires its derivative, velocity, which is already known, and does not require any computation. The formula for the acceleration vector is trivially obtained by manipulating the Lorentz force equation,

$$\mathbf{F} = m\mathbf{a} = q\mathbf{E} + q\mathbf{v} \times \mathbf{B} \tag{3.2}$$

where m is the mass of the particle.

$$\mathbf{a} = \frac{q\mathbf{E} + q\mathbf{v} \times \mathbf{B}}{m}. \tag{3.3}$$

With the above equation as the underlying trace-mechanism, particles can be simulated through Earth's magnetosphere, given magnetic and electric field models, by the following system of equations,

$$\dot{\mathbf{r}} = \mathbf{v} \tag{3.4}$$

$$\dot{\mathbf{v}} = \frac{q\mathbf{E} + q\mathbf{v} \times \mathbf{B}}{m}. \tag{3.5}$$

3.1.1   Magnetic Field

Although there are more complex magnetic field models, some of which are addressed later in this thesis, only a simple dipole will be considered for the full gyration model. This selection primarily serves to reduce computational costs, as the full gyration model is not an objective of this research, but rather a fundamental step towards a more efficient and comprehensive model. Furthermore, a dipole model of Earth's magnetic field is a useful and reasonable approximation at low L shells, albeit not the case at high L shells ([8], [21]). Utilizing this, comparisons can be made to some more extensive models with meaningful results.

Magnetic dipoles are a well understood concept, and the magnetic dipole moment generates a magnetic field that can be formulated as ([8], [21]),

$$\mathbf{B}(\mathbf{r}) = \frac{\mu_0}{4\pi} \left(\frac{3\mathbf{r}(\boldsymbol{\mu} \cdot \mathbf{r})}{r^5} - \frac{\boldsymbol{\mu}}{r^3} \right) \tag{3.6}$$

where $\mathbf{r}$ is the position vector of the particle, μ_0 is the vacuum permeability, $\boldsymbol{\mu}$ is the magnetic moment vector, and r is the radial distance of the particle from the origin of the dipole.

The implementation of a dipole magnetic field is simple and efficient. The function to compute the field only requires a vector containing the position of the particle, and along with some known constants, the field is explicitly calculated using the above formula (3.6).

3.1.2 Electric Field

The electric field in consideration is a combination of two factors: an electric field derived from the negative potential gradient, and the corotation electric field. The corotation electric field is simply the electric field due to the rotation of Earth, and it can be computed directly. The gradient of the electric potential is a more complicated matter, and requires a model of the electric potential. In the full gyration model, two potential models will be considered: a simple dipole-approximation model, and the more advanced Sojka model. In order to employ these potential models, the particle must be traced back to the Earth along the magnetic field lines to obtain a location on the surface, which can be computationally expensive. Such integration back to Earth's surface is viable since we assume that the electric potential is constant along magnetic field lines. This location on the surface serves as an input parameter to both the dipole and Sojka models, with which the electric potential is computed. These electric potentials are used to obtain the electric field vector, which is described in greater detail in the implementation section. Otherwise, the corotation electric field is explicitly computed throughout this thesis with a formula, which will be presented shortly.

The first component of the electric field is obtained by finding the gradient of the electric potentials. In the simple dipole-approximation model of the potentials, the tracing of the particles to the surface of Earth can be analytically determined. The analytic process for the trace is as follows ([8], [21]),

$$\lambda = \tan^{-1} \left(\frac{z}{||\mathbf{r}_{xy}||} \right), \tag{3.7}$$

$$L = \frac{||\mathbf{r}||}{\cos^2(\lambda)}, \tag{3.8}$$

$$\theta = \sin^{-1}\left(\sqrt{\frac{R_E}{L}}\right), \tag{3.9}$$

and

$$\phi = \text{atan}(y, x) \tag{3.10}$$

where x, y, z are the three components of the position vector $\mathbf{r}$, and $R_E = 6371000$ m is an Earth radii. The potential can be computed given spherical coordinates θ and ϕ (given $r = 1$). Furthermore, the potential at this point on Earth is the same as the potential of the original point in space since magnetic field lines are assumed to be equipotentials.

If a more complex magnetic field model is used, the above dipole-approximation analytic trace is no longer valid, and the particle must be numerically traced along magnetic field lines to the Earth's surface to obtain the θ and ϕ coordinates.

The corotation can be computed by ([8], [21]),

$$\mathbf{E}_{cor} = -\left(\left(\frac{2\pi\mathbf{z}}{24 \cdot 3600} \times \mathbf{r}\right) \times \mathbf{B}\right) \tag{3.11}$$

where $\mathbf{z}$ is a unit vector in the $+z$ direction. Only the internal component of the magnetic field, computed by the IGRF, is involved in this computation. Intuitively, the corotation electric field can be thought of as the electric field due to the rotation of Earth. That is, as Earth rotates, its magnetic axis rotates, and thus the fields also rotate. To be clear, imagine that the internal component of the magnetic field is a physical extension of the Earth. When the Earth rotates, the magnetic field will follow suit, with more distant points moving faster to maintain their relative position. This motion produces an Earthward electric field in a "stationary" (non-corotating) frame, this is the corotation electric field.

The overall electric field is the sum of the negative gradient of the potentials with the corotation electric field vector.

Using the dipole-approximation, the implementation is straightforward given the above formulas to determine θ and ϕ, as it only requires the position of the particle. The resulting θ and ϕ are plugged into a simple routine translated from Fortran code [12] to determine the potential. In order to acquire the gradient vector; however, the location in question must be axially perturbed, and the θ and ϕ recalculated. The purpose of this recalculation is to obtain the necessary values to apply finite difference methods to compute the derivative. Finite difference

methods are numerical implementations of the limit definition of the derivative,

$$f'(x) = \lim_{h \to 0} \frac{f(x+h) - f(x)}{h}$$

where we insert an appropriately small value for h such that a reasonable estimate of the derivative can be computed. Simple in concept, finite difference methods have proved effective in many numerical applications [9].

This perturb and recalculate process, in conjunction with finite difference methods, produces the electric field vector of the first component,

$$\mathbf{E}_{pot_x} = -\frac{P(\mathbf{r} + \mathbf{h}_x) - P(\mathbf{r})}{h} \tag{3.12}$$

where P is the potential and $\mathbf{h}_x = h\mathbf{i}$ is the small perturbation value in the x direction; this must be done for each of x, y, and z individually.

The second factor, the corotation electric field, is similarly simple to implement, requiring the position of the particle, and the magnetic field vector corresponding to the position, which was described above (3.11).

For the more advanced magnetic field models, the analytic tracing is replaced by a numerical tracing. This tracing can be implemented by solving the differential equation,

$$\dot{\mathbf{r}} = \pm \mathbf{B}(\mathbf{r}) \tag{3.13}$$

that is, tracing along the magnetic field lines to the surface of Earth. The sign of the magnetic field vector depends on the position of the particle, as the hemispherical symmetry of the Sojka model yields the same result tracing up or down the field lines. Using the z component of the particle position, we efficiently trace to the nearest hemisphere.

This method of integrating along the field lines must be performed four times per particle location to obtain the necessary values for finite differences, which yield the gradient. The numerous integrations occasionally result in undesirably long run-times, dependent on the initial particle location - which dictates how far the particle must be traced. The solution to overcome this, at the cost of some accuracy, is to construct a grid from which the electric field can be interpolated. The creation of the grid is computationally expensive, but does not add time to simulation once complete. Overall this leads to a reduction in run-time, assuming there are a sufficiently large number of simulations per grid. It is important to note that the 3D grid contains three values per point, the component-wise electric field values. This was found to best preserve accuracy, as opposed to storing the potential at each point. To provide an idea of the cost of constructing these grids, a $1001 \times 1001 \times 1001$ grid requires roughly 1920-2400 hours of process-

ing time.

Finally, the overall electric field **E** is obtained as the sum of the negative gradient of the electric potentials with the corotation electric field,

$$\mathbf{E} = \mathbf{E}_{pot} + \mathbf{E}_{cor}. \tag{3.14}$$

3.1.3 Overall Implementation

All models operate in the Geocentric Solar Magnetospheric coordinate system (GSM). The full gyration model accepts 3D velocity and position as the initializing input parameters. The model proceeds with a six-element state vector containing the position and velocity. The velocity is used to update the position, and the acceleration obtained from the Lorentz force equation (3.3) is used to update the velocity. Evaluations of the magnetic and electric fields in order to find the acceleration via the Lorentz force are the only computations that happen within the tracing function.

This model was first programmed in MATLAB. MATLAB has a variety of built-in integrators that are suitable for handling stiff and non-stiff problems. Although the built-in Dormand-Prince pair (explicit Runge-Kutta (4,5)), one-step solver ODE45 is the standard choice, the integration found improvement with the variable order Adams-Bashforth-Moulton PECE solver ODE113 [17]. An example simulation using the simple dipole-approximation is shown in Figure 3.1. Notice the gyrations, mirroring effect, and orbit of the particle.

3.2 Guiding Center Model

Tracing the gyrations is computationally expensive. Fortunately, the motion of the particle can be considered as the superposition of a relatively fast circular motion around a point called the guiding center and a relatively slow drift of this point. This idea was introduced in 1961 by Theodore Northrop [11]. By tracking the guiding center approximation as opposed to tracing the entirety of the particle's motion, we can achieve a significant reduction in computational cost.
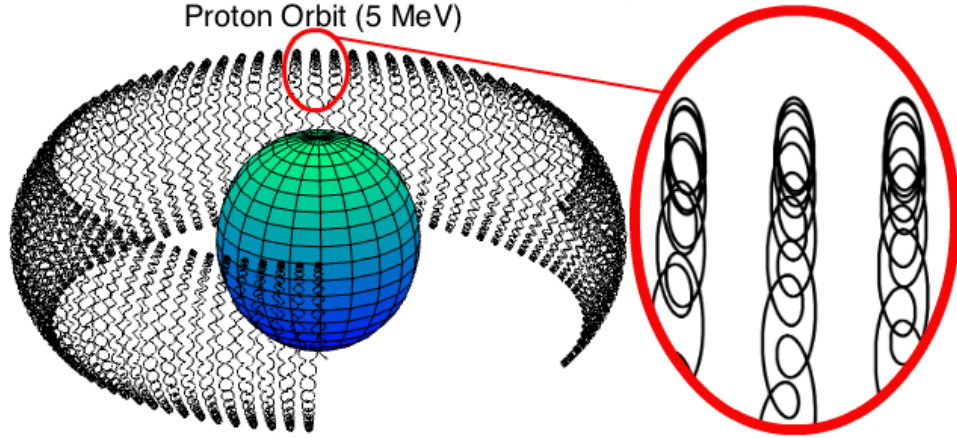
Figure 3.1: High energy proton orbiting Earth at three Earth radii (run time: 64.7 seconds, MATLAB).

In order to derive the guiding center equations, we begin by considering the Lorentz Force equation (note that we used [13] as a guide in these derivations),

$$\mathbf{F} = q\mathbf{E} + q\mathbf{v} \times \mathbf{B}. \tag{3.15}$$

This can be rewritten as,

$$m\mathbf{a} = q\mathbf{E} + q\mathbf{v} \times \mathbf{B}. \tag{3.16}$$

Dividing through by mass,

$$\mathbf{a} = \frac{q\mathbf{E}}{m} + \frac{q}{m}\mathbf{v} \times \mathbf{B}. \tag{3.17}$$

Now, consider the motion of the particle in the plane perpendicular to the magnetic field; the equation for the perpendicular motion is

$$\frac{d\mathbf{v}_\perp}{dt} = \frac{q\mathbf{E}_\perp}{m} + \frac{q}{m}\mathbf{v} \times \mathbf{B}. \tag{3.18}$$

Note that the acceleration $\mathbf{a}$ has been replaced by its equivalent definition, the derivative of velocity $\frac{d\mathbf{v}_\perp}{dt}$ (with respect to time). Also note that we can leave the velocity $\mathbf{v}$ alone in $\mathbf{v} \times \mathbf{B}$ since the parallel components will be eliminated by the cross product.

Next, we define $\mathbf{v}_\perp = \mathbf{u} + \mathbf{w}$ with a time-constant component $\mathbf{w}$, where $\mathbf{u}$

represents the circular motion. The equation becomes,

$$\frac{d(\mathbf{u} + \mathbf{w})}{dt} = \frac{q\mathbf{E}_\perp}{m} + \frac{q}{m}(\mathbf{u} + \mathbf{w}) \times \mathbf{B}. \tag{3.19}$$

Splitting the cross product and letting the time derivative of $\mathbf{w}$ disappear (since it's time-constant),

$$\frac{d\mathbf{u}}{dt} = \frac{q\mathbf{E}_\perp}{m} + \frac{q}{m}\mathbf{w} \times \mathbf{B} + \frac{q}{m}\mathbf{u} \times \mathbf{B}. \tag{3.20}$$

Choosing the velocity $\mathbf{w}$ such that $\frac{q\mathbf{E}_\perp}{m} + \frac{q}{m}\mathbf{w} \times \mathbf{B} = 0$ reduces the equation for $\mathbf{u}$ to the case with no electric force $\left(\frac{d\mathbf{u}}{dt} = \frac{q}{m}\mathbf{u} \times \mathbf{B}\right)$.

Solving for $\mathbf{w} = \mathbf{v}_E$,

$$\frac{q\mathbf{E}_\perp}{m} + \frac{q}{m}\mathbf{v}_E \times \mathbf{B} = 0, \tag{3.21}$$

$$\mathbf{E}_\perp + \mathbf{v}_E \times \mathbf{B} = 0. \tag{3.22}$$

If we let $\mathbf{v}_E = \mathbf{E} \times \mathbf{B}$, then we can apply the vector triple product and use the anticommutativity of cross products,

$$\mathbf{E}_\perp + (\mathbf{E} \times \mathbf{B}) \times \mathbf{B} = 0, \tag{3.23}$$

$$\mathbf{E}_\perp - (\mathbf{B} \cdot \mathbf{B})\mathbf{E}_\perp + (\mathbf{E}_\perp \cdot \mathbf{B})\mathbf{B} = 0. \tag{3.24}$$

Note that the parallel components of $\mathbf{E}$ are discarded by the cross product ($\mathbf{E}_\parallel \times \mathbf{B} = 0$), thus we can replace $\mathbf{E}$ with $\mathbf{E}_\perp$.

To deal with the magnitude being introduced let $B = \|\mathbf{B}\|$, and we redefine $\mathbf{v}_E = \frac{1}{B^2}\mathbf{E} \times \mathbf{B}$. The equation becomes,

$$\mathbf{E}_\perp - \frac{1}{B^2}(\mathbf{B} \cdot \mathbf{B})\mathbf{E}_\perp + \frac{1}{B^2}(\mathbf{E}_\perp \cdot \mathbf{B})\mathbf{B} = 0. \tag{3.25}$$

Using the properties of dot products,

$$\mathbf{E}_\perp - \mathbf{E}_\perp + \frac{1}{B^2}(\mathbf{E}_\perp \cdot \mathbf{B})\mathbf{B} = 0. \tag{3.26}$$

Finally, the electric and magnetic fields are orthogonal, thus their dot product is zero,

$$\mathbf{E}_\perp - \mathbf{E}_\perp = 0. \tag{3.27}$$

Thus, the definition for $\mathbf{v}_E$ satisfies the equation, and we have derived the first

guiding center equation; the equation for the electric field drift,

$$\mathbf{v}_E = \frac{1}{B^2}\mathbf{E} \times \mathbf{B}. \tag{3.28}$$

In order to derive the remaining two guiding center equations of interest, we first must define and derive a few supplementary ideas and equations. We begin by deriving the equation for a general force.

For a general force in the Lorentz equation, we can substitute $\mathbf{F} = q\mathbf{E}$, where $\mathbf{F}$ is a general constant force term.

$$\frac{d\mathbf{v}}{dt} = \frac{1}{m}\mathbf{F} + \frac{q}{m}\mathbf{v} \times \mathbf{B}. \tag{3.29}$$

Following a similar route as when deriving the first guiding center equation, we define $\mathbf{v} = \mathbf{u} + \mathbf{w}$ with a time-constant component $\mathbf{w}$, and component $\mathbf{u}$ representing the circular motion. The equation becomes,

$$\frac{d(\mathbf{u} + \mathbf{w})}{dt} = \frac{1}{m}\mathbf{F} + \frac{q}{m}(\mathbf{u} + \mathbf{w}) \times \mathbf{B}. \tag{3.30}$$

Splitting the cross product and letting the derivative of $\mathbf{w}$ disappear,

$$\frac{d\mathbf{u}}{dt} = \frac{1}{m}\mathbf{F} + \frac{q}{m}\mathbf{w} \times \mathbf{B} + \frac{q}{m}\mathbf{u} \times \mathbf{B}. \tag{3.31}$$

Choosing the velocity $\mathbf{w}$ such that $\frac{1}{m}\mathbf{F} + \frac{q}{m}\mathbf{w} \times \mathbf{B} = 0$ reduces the equation for $\mathbf{u}$ to the case with no electric force $\left(\frac{d\mathbf{u}}{dt} = \frac{q}{m}\mathbf{u} \times \mathbf{B}\right)$.

Solving for $\mathbf{w} = \mathbf{v}_F$,

$$\frac{1}{m}\mathbf{F} + \frac{q}{m}\mathbf{v}_F \times \mathbf{B} = 0, \tag{3.32}$$

$$\mathbf{F} + q\mathbf{v}_F \times \mathbf{B} = 0. \tag{3.33}$$

Based on the previous derivation, we let $\mathbf{v}_F = \frac{1}{qB^2}\mathbf{F} \times \mathbf{B}$, then we can apply the vector triple product and use the anticommutativity of cross products to check if the equation is satisfied,

$$\mathbf{F} + q\left(\frac{1}{qB^2}\mathbf{F} \times \mathbf{B}\right) \times \mathbf{B} = 0, \tag{3.34}$$

$$\mathbf{F} + \frac{1}{B^2}\left(\mathbf{F} \times \mathbf{B}\right) \times \mathbf{B} = 0, \tag{3.35}$$

$$\mathbf{F} - \frac{1}{B^2}(\mathbf{B} \cdot \mathbf{B})\mathbf{F} + \frac{1}{B^2}(\mathbf{F} \cdot \mathbf{B})\mathbf{B} = 0. \tag{3.36}$$

Using the properties of dot products,

$$\mathbf{F} - \mathbf{F} + \frac{1}{B^2}(\mathbf{F} \cdot \mathbf{B})\mathbf{B} = 0. \tag{3.37}$$

Finally, by definition the general force term $\mathbf{F}$ and the magnetic field are orthogonal, thus their dot product is zero,

$$\mathbf{F} - \mathbf{F} = 0. \tag{3.38}$$

Thus, the definition for $\mathbf{v}_F$ satisfies the equation, and we have derived the drift produced by a general force term,

$$\mathbf{v}_F = \frac{1}{qB^2}\mathbf{F} \times \mathbf{B}. \tag{3.39}$$

Having acquired an equation for the drift produced by a general force term, we need to derive a few more things.

Let's begin by considering a particle moving through a uniform magnetic field, it will experience a force given by the Lorentz equation,

$$\mathbf{F} = q\mathbf{v} \times \mathbf{B}. \tag{3.40}$$

Since this force is the cross product of the velocity and the magnetic field, it will act in the direction orthogonal to the motion of the particle and magnetic field, causing a circular gyration. The radius of this gyration r_g can be computed by equating the centripetal force with the magnitude of the Lorentz force,

$$F_c = \frac{mv_\perp^2}{r_g} = |q\mathbf{v} \times \mathbf{B}| = |q|v_\perp B \tag{3.41}$$

where $v_\perp$ is the magnitude of the perpendicular velocity.

Solving for r_g yields an expression for the gyroradius,

$$r_g = \frac{mv_\perp}{|q|B}. \tag{3.42}$$

Given the gyroradius, we can compute the period T_g as the gyration's circumference divided by the speed,

$$T_g = \frac{2\pi r_g}{v_\perp}. \tag{3.43}$$

Furthermore, we can compute the frequency ω_g from the period,

$$\omega_g = \frac{2\pi}{T_g} = \frac{|q|B}{m}. \tag{3.44}$$

With these at hand, we seek to derive the magnetic moment, and the force produced by the magnetic moment.

The magnetic moment of a closed current loop is given by,

$$\mu = \frac{1}{2}I \oint_C \mathbf{r} \times d\mathbf{l} \tag{3.45}$$

with the current I, position vector $\mathbf{r}$, and closed contour C. The current is the charge divided by the gyro-period,

$$I = \frac{|q|}{T_g} = \frac{|q|\omega_g}{2\pi}. \tag{3.46}$$

The line integral $\frac{1}{2}\oint_C \mathbf{r} \times d\mathbf{l}$ is the area of the circle enclosed by the gyro motion,

$$A = \frac{1}{2} \oint_C \mathbf{r} \times d\mathbf{l} = \pi r_g^2. \tag{3.47}$$

Combining these yields a result for the magnetic moment,

$$\mu = IA = \left(\frac{|q|\omega_g}{2\pi} \right) \left(\pi r_g^2 \right). \tag{3.48}$$

Using the definition of the gyro radius r_g and the frequency ω_g,

$$\mu = \left(\frac{|q|^2 B}{2\pi m} \right) \left(\pi \frac{m^2 v_\perp^2}{|q|^2 B^2} \right). \tag{3.49}$$

Simplifying we obtain our final expression for the magnetic moment,

$$\mu = \frac{1}{2} \frac{m v_\perp^2}{B}. \tag{3.50}$$

In vector form, the magnetic moment is anti-aligned with the magnetic field (by right-hand rule),

$$\boldsymbol{\mu} = \frac{1}{2} \frac{m v_\perp^2}{B} \left(-\frac{\mathbf{B}}{B} \right) = -\frac{m v_\perp^2}{2B} \frac{\mathbf{B}}{B}. \tag{3.51}$$

To compute the force produced by the magnetic moment, we begin by consider-

21

ing the Lorentz force on a current loop,

$$\mathbf{F}_{\mu} = \nabla(\boldsymbol{\mu} \cdot \mathbf{B}). \tag{3.52}$$

Substituting our definition of the magnetic moment,

$$\mathbf{F}_{\mu} = \nabla\left(-\frac{mv_{\perp}^2}{2B}\frac{\mathbf{B}}{B} \cdot \mathbf{B}\right). \tag{3.53}$$

Using the definition of the dot product,

$$\mathbf{F}_{\mu} = \nabla\left(\left|-\frac{mv_{\perp}^2}{2B}\frac{\mathbf{B}}{B}\right||\mathbf{B}|\cos\theta\right) \tag{3.54}$$

where θ is the angle between the two vectors, which is $\theta = \pi$ due to the anti-alignment. Evaluating the cosine and moving the constants to the front,

$$\mathbf{F}_{\mu} = \nabla\left(-\left|-\frac{mv_{\perp}^2}{2B}\right|\left|\frac{\mathbf{B}}{B}\right||\mathbf{B}|\right), \tag{3.55}$$

$$\mathbf{F}_{\mu} = -\frac{mv_{\perp}^2}{2B}\nabla\left(\left|\frac{\mathbf{B}}{B}\right||\mathbf{B}|\right). \tag{3.56}$$

Note that the constant term in question is the magnetic moment, which is conserved. It will always be constant regardless of changes to the magnetic field or perpendicular velocity (the perpendicular velocity will change corresponding to the change in the magnetic field such that the magnetic moment is conserved, and vice-versa), this allows the constant to be pulled out of the gradient operation.

Since $\frac{\mathbf{B}}{B}$ is a unit vector, its magnitude is one (also recall $|\mathbf{B}| = B$),

$$\mathbf{F}_{\mu} = -\frac{mv_{\perp}^2}{2B}\nabla(B). \tag{3.57}$$

Taking the gradient, we acquire the force produced by the magnetic moment,

$$\mathbf{F}_{\mu} = -\frac{mv_{\perp}^2}{2B}\nabla B. \tag{3.58}$$

With these equations we proceed to derive the magnetic gradient drift.

In the presence of a magnetic gradient, the force in the Lorentz equation is

the force due to the magnetic moment on the guiding center,

$$\mathbf{F}_\mu = -\frac{mv_\perp^2}{2B} \nabla B \tag{3.59}$$

Recall the general force drift,

$$\mathbf{v}_F = \frac{1}{qB^2} \mathbf{F} \times \mathbf{B}. \tag{3.60}$$

Substituting the force due to the magnetic moment, we obtain the formula,

$$\mathbf{v}_G = \frac{1}{qB^2} \left(-\frac{mv_\perp^2}{2B} \nabla B \right) \times \mathbf{B}. \tag{3.61}$$

Simplifying, and canceling the negative using the anti commutativity of cross products, we obtain the final expression for the magnetic gradient drift,

$$\mathbf{v}_G = \frac{mv_\perp^2}{2qB^3} \left(\mathbf{B} \times \nabla B \right). \tag{3.62}$$

The third guiding center equation we seek to derive accounts for the drift velocity produced by the curvature force. Consider the centrifugal force,

$$F_c = \frac{mv_\parallel^2}{r_c} \tag{3.63}$$

where r_c is the magnitude of the radius of curvature vector $\mathbf{r}_c$. In vector form,

$$\mathbf{F}_c = mv_\parallel^2 \frac{\mathbf{r}_c}{r_c^2}. \tag{3.64}$$

With this in mind, we define a local coordinate system with components (see Figure 3.2),

$$\mathbf{e}_1 = \frac{\mathbf{B}}{B}, \tag{3.65}$$

$$\mathbf{e}_2 = -\frac{\mathbf{r}_c}{r_c}. \tag{3.66}$$

By these definitions, $\mathbf{e}_1$ is the tangent vector to $\mathbf{B}$, and $\mathbf{e}_2$ is the normal vector to $\mathbf{B}$ passing through the guiding center. It follows from calculus that the derivative of the tangent vector is the normal vector (including a normalizing factor, in this
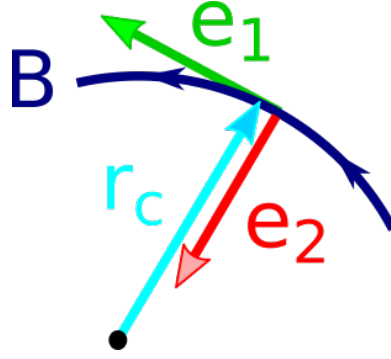
Figure 3.2: Visualization of the defined local coordinate system.

case, the radius of the circle),

$$\frac{\partial \mathbf{e}_1}{\partial s} = \frac{\mathbf{e}_2}{r_c} \tag{3.67}$$

where s is the line element along the field line.

Using the definitions of the coordinate system,

$$\frac{\partial}{\partial s}\left(\frac{\mathbf{B}}{B}\right) = -\frac{\mathbf{r}_c}{r_c^2}. \tag{3.68}$$

We solve to obtain an expression for the $\frac{\mathbf{r}_c}{r_c^2}$ term,

$$\frac{\mathbf{r}_c}{r_c^2} = -\frac{\partial}{\partial s}\left(\frac{\mathbf{B}}{B}\right). \tag{3.69}$$

Using the quotient rule and simplifying,

$$\frac{\mathbf{r}_c}{r_c^2} = -\left(\frac{B\frac{\partial \mathbf{B}}{\partial s} - \mathbf{B}\frac{\partial B}{\partial s}}{B^2}\right), \tag{3.70}$$

$$\frac{\mathbf{r}_c}{r_c^2} = \frac{\mathbf{B}}{B^2}\frac{\partial B}{\partial s} - \frac{1}{B}\frac{\partial \mathbf{B}}{\partial s}. \tag{3.71}$$

This yields a new expression for the $\frac{\mathbf{r}_c}{r_c^2}$ term that will eventually be used in the centrifugal force.

To evaluate the rightmost term, consider the partial derivative $\frac{\partial \mathbf{B}}{\partial s}$. We begin by using the Chain rule to expand the partial derivative,

$$\frac{\partial \mathbf{B}}{\partial s} = \frac{\partial \mathbf{B}}{\partial x}\frac{\partial x}{\partial s} + \frac{\partial \mathbf{B}}{\partial y}\frac{\partial y}{\partial s} + \frac{\partial \mathbf{B}}{\partial z}\frac{\partial z}{\partial s}. \tag{3.72}$$

Since s represents the arc length parameter along the magnetic field line, it follows from the differential equations that $\frac{\mathbf{B}}{B} = \langle \frac{\partial x}{\partial s}, \frac{\partial y}{\partial s}, \frac{\partial z}{\partial s} \rangle$,

$$\frac{\partial \mathbf{B}}{\partial s} = \frac{1}{B}\frac{\partial \mathbf{B}}{\partial x}B_x + \frac{1}{B}\frac{\partial \mathbf{B}}{\partial y}B_y + \frac{1}{B}\frac{\partial \mathbf{B}}{\partial z}B_z \tag{3.73}$$

where the subscripts indicate the component of a vector (as opposed to a partial derivative).

This can be written in vector form,

$$\begin{aligned}\frac{\partial \mathbf{B}}{\partial s} = \Big\langle &\frac{1}{B}B_x\frac{\partial B_x}{\partial x} + \frac{1}{B}B_y\frac{\partial B_x}{\partial y} + \frac{1}{B}B_z\frac{\partial B_x}{\partial z}, \\ &\frac{1}{B}B_x\frac{\partial B_y}{\partial x} + \frac{1}{B}B_y\frac{\partial B_y}{\partial y} + \frac{1}{B}B_z\frac{\partial B_y}{\partial z}, \\ &\frac{1}{B}B_x\frac{\partial B_z}{\partial x} + \frac{1}{B}B_y\frac{\partial B_z}{\partial y} + \frac{1}{B}B_z\frac{\partial B_z}{\partial z}\Big\rangle.\end{aligned} \tag{3.74}$$

By definition, this is equivalent to

$$\frac{\partial \mathbf{B}}{\partial s} = \frac{1}{B}(\mathbf{B} \cdot \nabla)\mathbf{B}. \tag{3.75}$$

Using this, we obtain a final version for our expression,

$$\frac{\mathbf{r}_c}{r_c^2} = \frac{\mathbf{B}}{B^2}\frac{\partial B}{\partial s} - \frac{1}{B^2}(\mathbf{B} \cdot \nabla)\mathbf{B}. \tag{3.76}$$

Substituting this expression into our equation for the centrifugal force,

$$\mathbf{F}_c = mv_\parallel^2 \left(\frac{\mathbf{B}}{B^2}\frac{\partial B}{\partial s} - \frac{1}{B^2}(\mathbf{B} \cdot \nabla)\mathbf{B}\right). \tag{3.77}$$

Applying this force to the equation for drift from a general force term,

$$\mathbf{v}_C = \frac{1}{qB^2}\left(mv_\parallel^2\left(\frac{\mathbf{B}}{B^2}\frac{\partial B}{\partial s} - \frac{1}{B^2}(\mathbf{B} \cdot \nabla)\mathbf{B}\right)\right) \times \mathbf{B}. \tag{3.78}$$

The first term in the inner most set of parenthesis is a constant multiplied with $\mathbf{B}$. This term will disappear when evaluating the cross product with $\mathbf{B}$ (since $\mathbf{B} \times \mathbf{B} = 0$) leaving,

$$\mathbf{v}_C = \frac{1}{qB^2}\left(-mv_\parallel^2\frac{1}{B^2}(\mathbf{B} \cdot \nabla)\mathbf{B}\right) \times \mathbf{B}. \tag{3.79}$$

Simplifying and using the anti-commutativity of cross products, we acquire the guiding center equation for the curvature drift,

$$\mathbf{v}_C = \frac{mv_\parallel^2}{qB^4}\mathbf{B} \times [(\mathbf{B} \cdot \nabla)\,\mathbf{B}]. \tag{3.80}$$

The final equation that needs to be derived regards the parallel velocity. In order to update the parallel velocity in the simulation, we need to determine an expression for its derivative. We begin by considering the force due to the magnetic moment on the guiding center (3.58),

$$\mathbf{F}_\mu = -\frac{mv_\perp^2}{2B}\nabla B. \tag{3.81}$$

The component of this which is perpendicular to the magnetic field results in the gradient drift. The component which is parallel to the magnetic field accelerates the particle along the magnetic field. Considering the parallel component of this force,

$$\mathbf{F}_\parallel = \left(-\frac{mv_\perp^2}{2B}\nabla B\right)_\parallel. \tag{3.82}$$

This can be used to solve for the parallel acceleration, which is equivalent to the derivative of the parallel velocity,

$$\mathbf{F}_\parallel = m\mathbf{a}_\parallel = m\dot{\mathbf{v}}_\parallel = \left(-\frac{mv_\perp^2}{2B}\nabla B\right)_\parallel, \tag{3.83}$$

$$\dot{\mathbf{v}}_\parallel = \frac{\left(-\frac{mv_\perp^2}{2B}\nabla B\right)_\parallel}{m}. \tag{3.84}$$

Moving the constant out to the front,

$$\dot{\mathbf{v}}_\parallel = \frac{-\frac{mv_\perp^2}{2B}(\nabla B)_\parallel}{m}. \tag{3.85}$$

The constant in the numerator is the negative magnetic moment (3.50),

$$\dot{\mathbf{v}}_\parallel = \frac{-\mu\,(\nabla B)_\parallel}{m}. \tag{3.86}$$

The parallel component of the gradient can be simplified by noting that we seek

an expression for the derivative of the scalar-valued parallel velocity, that is,

$$\dot{v}_{\parallel} = \frac{-\mu \left(\frac{\mathbf{B}}{B} \cdot \nabla B \right)}{m}. \tag{3.87}$$

Since the desired quantity is a scalar, we can compute the parallel component (with respect to the magnetic field) of the gradient by taking the dot product with a unit vector in the direction of the magnetic field. This leaves us with our final equation for the derivative of the parallel velocity,

$$\dot{v}_{\parallel} = -\frac{\mu}{m} \left(\frac{\mathbf{B}}{B} \cdot \nabla B \right). \tag{3.88}$$

The three guiding center equations are defined by constants in combination with the electric and magnetic field vectors, as well as the parallel and perpendicular velocity. The gradients in the equations are again computed using finite difference methods. As for the model, the input parameters are energy, pitch angle, and position. The state vector has evolved to contain the 3D position and the scalar-valued parallel velocity. The perpendicular velocity is calculated as the sum,

$$\mathbf{v}_{\perp} = \mathbf{v}_E + \mathbf{v}_G + \mathbf{v}_C, \tag{3.89}$$

with an initial value assignment before the integration.

The integration follows a tracing function that computes the magnetic and electric fields, applies the resulting vectors to obtain the guiding center velocities using formulas (3.28), (3.62), and (3.80), then updates the position by summing the perpendicular and parallel velocities (the parallel scalar velocity is applied to a unit vector in the direction of the magnetic field). The parallel velocity is updated via the equation above (3.88). Altogether, the state vector is updated by the following system of equations,

$$\dot{\mathbf{r}} = \mathbf{v}_{\perp} + \left(\frac{\mathbf{B}}{B} \right) v_{\parallel}, \tag{3.90}$$

$$\dot{v}_{\parallel} = -\frac{\mu}{m} \left(\frac{\mathbf{B}}{B} \cdot \nabla B \right). \tag{3.91}$$

The simple dipole-approximation of the guiding center was first implemented in MATLAB, with an additional version in C. The C version of the code utilizes the SUNDIALS library for integration. SUNDIALS stands for SUite of Nonlinear and DIfferential/ALgebraic Equation Solvers and is made freely available by Lawrence Livermore National Laboratory [7]. Multiple methods of integration are available, but the results best matched those previously computed by MAT-

LAB when using the Adams-Moulton method. A comparative sample simulation is featured below (see Figure 3.3). Notice the gyrations, which accounted for much of the computing power, are no longer present, but the mirroring effect and orbit remain. Also notice the difference in run time between the guiding center (Figure 3.3) and the full gyration (Figure 3.1) simulation. While the full model requires over a minute, the guiding center model requires just over ten seconds, meaning a reduction in computation by a factor of six.
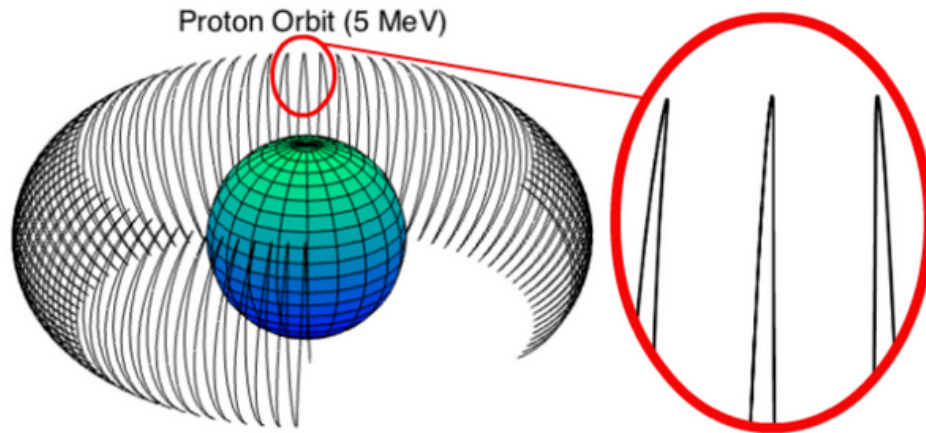

Figure 3.3: High energy proton orbiting Earth at three Earth radii (run time: 10.8 seconds, MATLAB).

3.2.1 Advanced Magnetic Field

The magnetic field model used in many practices is a combination of the International Geomagnetic Reference Model (for internal sources) and the Tsyganenko model (for external sources). These models are freely available in FOR-TRAN.

The International Geomagnetic Reference Model and Tsyganenko model are best-fit approximations to a large number of satellite observations ([22], [23]). This thesis uses the IGRF2008 and Tysganenko T89c models. The IGRF models are based on a spherical harmonic series, which was shown to represent the main geomagnetic field by Carl Friedrich Gauss in 1839. The difference between IGRF models is in the form of updated coefficients, based on the inclusion of new data. These data typically come from magnetic observatories, measurement stations, surveys from aircrafts and ships, and global satellite measurements. The number

attached after IGRF represents the year the model was issued, in the case of this thesis, 2008.

The Tsyganenko models vary, in one sense, by focus. The 1996 Tsyganenko model focuses on accurately modeling the magnetopause, while the Tsyganenko 1989 model T89c bins the data by K_p and is useful when K_p is of primary importance. Since we are interested in the effects of varying K_p, it is most sensible to select the T89c model for the purposes of this thesis.

Many useful codes including the aforementioned IGRF2008 can be obtained with the GEOPACK modeling software package [24], in addition to stand-alone Tsyganenko models, all provided by the Community Coordinated Modeling Center (CCMC) connected to NASA.

In order to utilize the IGRF2008 and T89c models, a number of internal variables must be initialized, which requires the knowledge of solar wind velocity and time. The time requested by the model includes year, day, hour, minute, and second. This is for modeling the orientation of the magnetic axis. The solar wind velocity is requested by component in x, y, and z. The selected time is fixed uniquely for each simulation, as days will be selected based on desired conditions. The solar wind velocity is fixed at the standard values of zero in y and z, and -400 km/s in x.

Given this information, the internal variables can be set, but to run the magnetic field computing functions within the T89c model, the IOPT (essentially a shifted version of K_p), particle position, and tilt angle of Earth must be provided. While K_p is varied in different simulations, the particle position is known by the outside integration, and the tilt angle of Earth is computed by the date and time. The function that computes this tilt angle is separately included with the GEOPACK package.

3.2.2   Advanced Electric Field

The electric field is generated from tracing along magnetic field lines back to Earth's surface. The Sojka model is used to compute the surface potentials whose values are again extended to the trace origin in space.

The advanced electric field is generated similarly to that of the previously discussed electric fields. It begins with the generation of a $1001 \times 1001 \times 1001$ semi-logarithmically spaced, spherical grid extending from the surface of the Earth to 15 Earth radii. Each location is traced back to the surface of Earth using the IGRF and Tysganenko models as the driving force. This occurs three more times at perturbed versions of the original location to obtain four traced

locations on Earth's surface. These four locations are input to the Sojka model to obtain estimates of the potentials. The four potentials are the values needed for finite difference methods to compute the gradient. The negative gradient of the potential is the electric field which is stored at each location.

3.2.3 Overall Implementation

The entirety of the simulation code is run on a computer cluster utilizing ten blades of twelve cores each. The code requires initial energy, pitch angle, and position to begin simulation. Once these inputs have been provided, the SUNDIALS integrator is initialized with the desired method of integration, tolerances, state vector, output time step, special conditions (intersection with the leading satellite), and termination conditions. The integration method was selected such that the error between the simpler MATLAB and C models was minimized. To determine an appropriate tolerance, simulations were run for decreasing tolerances, and the point where error was no longer meaningfully reduced was selected as the tolerance to be used. The state vector consists of the same values as in the second model: the position vector and scalar-valued parallel velocity. The position will be carefully set to specific locations on the trailing Van Allen satellite's position. The parallel velocity is initially computed from the input energy and pitch angle. The output time step is set to an arbitrarily large value to speed up simulation, as a small output time step requests intermediary points which forces the integrator to stop and interpolate values before continuing. By selecting an arbitrarily large output time step, the integrator can operate freely until a special or termination condition occurs. The special condition that will be searched for is intersection with the leading Van Allen satellite's orbit.

Finding the intersection of a simulated particle with a satellite orbit is nontrivial, as the chance of such a collision is practically negligible. In order to determine the special condition, that is, where the particle intersects the orbit (or any magnetic field line extending from the orbit) of the leading satellite, a boundary is introduced. This boundary is a three dimensional surface mapping the satellite orbit along the magnetic field lines both up and down to Earth's surface (see Figure 3.4). The design of such a boundary around a satellite orbit (which is not too similar to the orbit of a particle) nearly ensures intersection at some point in a particle's trajectory.

Once a particle has intersected with the boundary, the satellite orbit location which generated said boundary intersection point is credited with intersection with the particle. This is sensible as the particle is representative of a stream of similar particles that exist along the same magnetic field line. It should be noted
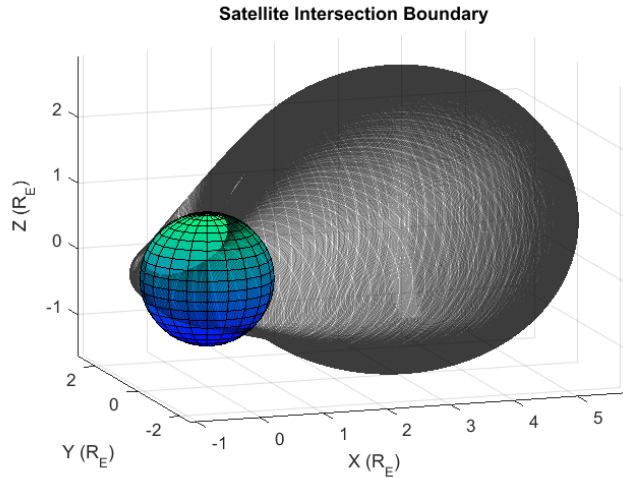
Satellite Intersection Boundary

Figure 3.4: Leading satellite boundary. The surface formed by integrating along magnetic field lines to Earth's surface.

that multiple intersections can occur, all of which are recorded and treated as unique pairs.

The primary stopping condition for the integration is return of the particle to its starting azimuthal location, in addition to the aforementioned termination conditions. This allows for one orbit of the particle, whereas no new information should be gained beyond the first orbit as the fields are static.

Once the integrator has been fully initialized, it begins tracing of the particle by computing the magnetic and electric field vectors using the advanced models. The magnetic field vector is obtained by calling the IGRF and Tsyganenko Fortran codes discussed previously. The electric field, however, is stored as a 24 GB grid. In order for the computer cluster simulating the particle motion to utilize the grid, it must first load the grid into memory; however, it is not feasible on the given machine nor generally reasonable to load a 24 GB grid multiple times. As a result, a single copy of the grid is stored into shared memory, where it can be accessed by all of the running programs simultaneously, which use the grid to interpolate the electric field vector.

With the electric and magnetic field vectors known, the guiding center velocities and parallel velocity derivative can be computed and used to update the state vector. This is repeated until the aforementioned boundary is intersected, at which point all relevant information is recorded, after which it continues until it reaches another intersection, a special termination condition, or until the particle azimuth returns to its initial value.

CHAPTER 4

SIMULATION SETUP AND DATA PREPARATION

4.1 Selection of the Day

Given that the model assumes time stationarity (that is, effects on the magnetic and electric field due to time are assumed to be negligible), a day of consistent K_p must be selected to ensure that the fields are not changing significantly within the simulation. Days which maintain a constant K_p for a minimum of 12 consecutive hours meet this criteria, provided that the real-time within the simulation is expected to be on the order of hours. Additionally, the selected day must have complete data for both satellites; there are periods of time in which the satellites do not report data as well as periods of time with few measurements (the satellite reports failed measurements). Furthermore, both satellites must be roughly equatorial, that is, approximately near the magnetic field minimum surface. If the satellites deviate up or down while maintaining radial distance, then the data is actually measuring particles traveling along radially more distant paths, which lessens the results from simulation, as the particle populations that are more distant are more prone to leaving the magnetosphere. Lastly, one satellite should be positioned on the outgoing pass away from Earth, and the other on the incoming pass towards Earth. This both observes a more complex domain of the magnetic field and avoids the near-Earth region which would produce predictably insensitive results, due to the K_p parameter typically impacting the tail of the magnetosphere more.

In order to verify the model, two days of low and medium K_p were selected. (Note that high K_p days seldom occur - although there are geomagnetic storms, they rarely result in a 12 hour period of consistently high K_p, which was a specified requirement for the assumption of time stationarity.) The selected low K_p time interval was March 7th, 2014, centered around 12 UTC. The medium K_p time interval was February 21st, 2014, around 0 UTC. The observed K_p plots pulled directly from the Van Allen Probes Science Gateway database are shown in Figures (4.1, 4.2).
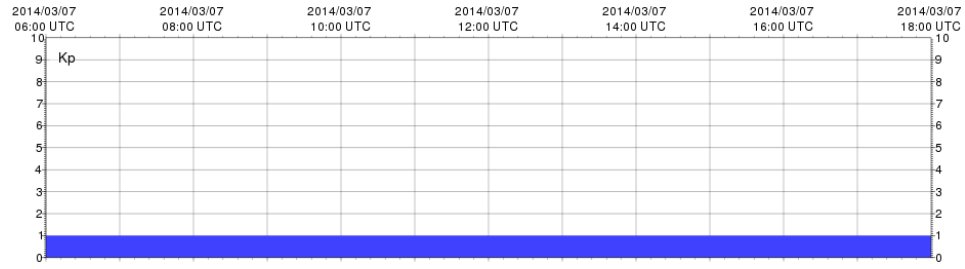
Figure 4.1: The observed low K_p in the selected time period generated by the RBSP database.
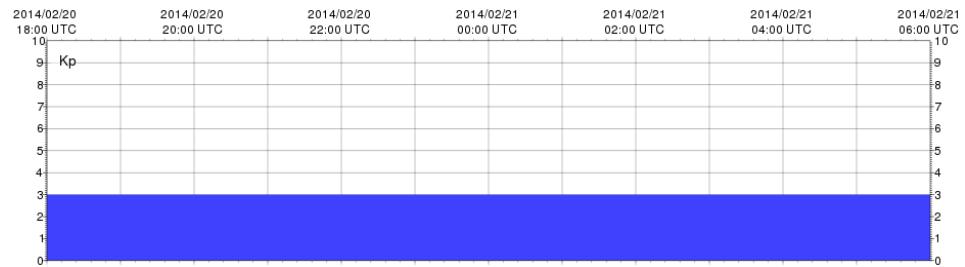

Figure 4.2: The observed medium K_p in the selected time period generated by the RBSP database.

Within these days lie desirably equatorial orbits, which are expected to yield the most results. The orbits of the satellites' are nearly-identical, but delayed; the orbits and most equatorial orbit of the satellites are featured in the following Figures (4.3, 4.4).
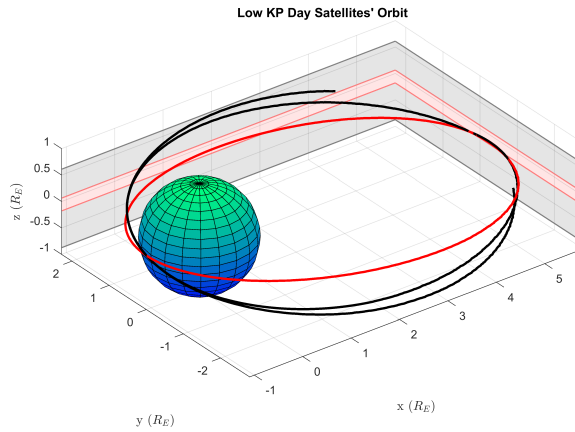
Figure 4.3: The orbital path of the satellites (black) and most equatorial orbit (red), including the variation on the equatorial axis (shaded regions) for the low K_p day; GSM coordinate system.
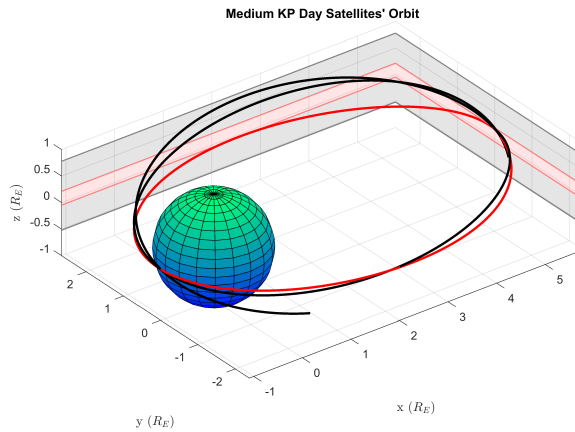
Figure 4.4: The orbital path of the satellites (black) and most equatorial orbit (red), including the variation on the equatorial axis (shaded regions) for the medium K_p day; GSM coordinate system.

Beyond the satisfaction of the two aforementioned criteria, the time at which the satellites are on the outgoing and incoming pass can be chosen as the center for computation. Finally, both satellites have complete data for the selected days, which will be illustrated in the following section.

4.2   Particle Spawning

In order to obtain complete coverage of the fields and their changes with respect to K_p, we spawn an ensemble of particles of various energies and pitch angles at various positions. Although this was initially done uniformly across the satellite path, including a uniform spread of energies and pitch angles, the process was streamlined to target features of the satellite spectrograms. The focus eventually materialized in the form of vertical and horizontal line plots. These were selected due to their computational feasibility in conjunction with their reasonably informative results. Beyond this, features of the spectrograms are expected to change or shift with respect to K_p. Line plots are an ideal method for taking one such slice of a feature, whereas simulating the entire region is frequently redundant and to reiterate, computationally demanding. This decision is further supported by the convenient structure of the features - they have primarily straight edges parallel to the cardinal axes, meaning that simple horizontal and vertical line plots are near-normal to the features' surfaces, which is ideal. Ultimately, the objective is to produce measurably different results for different K_p values, which these boundaries (features) may serve as the best source of change. Accordingly, particles along three particular energies and three particular positions were spawned to create the aforementioned horizontal and vertical lines, respectively. These energies and positions were selected because they cross key features of interest. A depiction of the spawn lines is included as Figure (4.5).

The dimensions of the spectrogram are 72 rows by 1284 columns. Furthermore, every point corresponds to 11 particles of identical position and energy, but varying pitch angle. It follows that the total number of particles in a vertical line is 792. Altogether that's almost 2400 spawns for the vertical lines alone. A horizontal line at full resolution requires over 14,000 particle simulations, which would require many weeks if not months to fully compute. However, the main feature these horizontal lines are meant to observe is the initial vertical wall just past 2.7 R_E (on the left side) on the position axis. Rather than pursue a full horizontal line at low resolution, it was decided to simulate a small portion around the feature of interest at high resolution. A small number of points were logarithmically spaced, slightly distant from the feature, whereas nearby was full resolution - requiring a little under 80 position-energy points to simulate. In other words, the vertical and horizontal line plots consist of roughly the same number of points, both of which fall into the category of computationally reasonable.
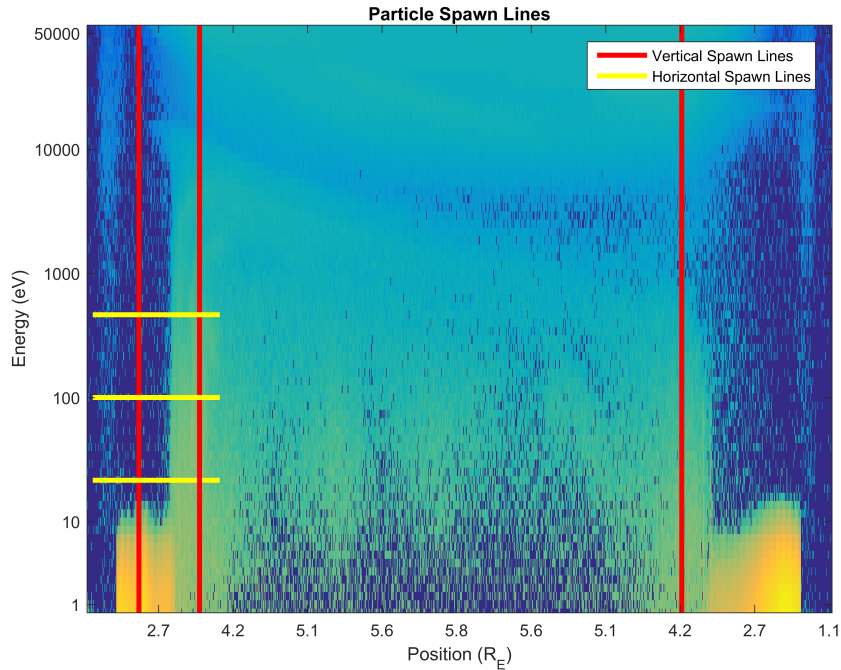
Figure 4.5: The regions of interest (shaded yellow and red) encompassing spectrogram features in which particles are spawned.

4.3 Termination Conditions

The total 4,917 particles were simulated until one of the following conditions was met: the initial azimuth was reached, the particle entered Earth, the particle exceeded 15 Earth radii, the real-time within simulation surpassed 24 hours, or SUNDIALS returned failure from the integration. Although additional termination conditions were applied to other simulations and testing, such as limiting the number of reported intersections or defining a maximum number of integration steps, these were excluded in the final, full simulations, as they serve to reduce simulation time with minimal impact on the results.

By halting the particle simulation at the initial azimuth, we restrict the particle to a single orbit. Theoretically the second orbit would follow roughly the same path as the first orbit (provided the model is time-stationary), yielding no new results. Thus we reduce simulation time without loss of data by constraining the motion to one orbit.

Although we do not expect the position of any particle to decrease below

one Earth radii, it is not infeasible given the slight error in numerical integration, especially with respect to the particles that were spawned near Earth. Physically, particles cannot enter Earth, thus we include such a bound as a safety measure. Similarly, particles are known to sometimes diverge and travel far outside the region of interest. The particles frequently do not return, and the simulation time required is dramatically increased in correspondence to the length of the diverging particle path. As such, it is sensible to include an upper bound of 15 Earth radii; large enough such that some particles that do simulate to more distant radii have enough space to return, while those which are highly unlikely to return and surpass 15 Earth radii are dropped.

Lastly, it is necessary to limit the simulated real-time. Not only does this reinforce the assumption of time stationarity, but it also saves a potentially immense amount of simulation time. Some low energy particles are particularly slow in their orbit, and it can be very costly to attempt to simulate the entire path.

Given these termination conditions, the particles simulate freely, unrestricted in their intersections with the leading satellite's magnetic boundary. Every intersection is recorded and used when processing the results.

4.4   Simulation Output

Out of the 4,917 particles simulated, none were guaranteed to successfully intersect the path (magnetic boundary) of the leading satellite (see Figure 3.4 in Chapter 3). However, some particles were observed to intersect the boundary more than once - all of which were recorded. For each instance of intersection, the simulation recorded the initial and final energy, pitch angle, and position (subtotal of ten values), as well as the point of satellite intersection, the 2-norm of the magnetic field at that point, and the parallel velocity. The use of each of these values will be explained in the following section on post processing. Although the simulation also returned lists of other values, these values sole purpose was to indicate how the simulation terminated, along with any errors that may have occurred. Each of the aforementioned lines of data were printed to individual files, which were directly used in the post-processing.

4.5   Post-Processing

As mentioned in the previous section, the output from the simulations was multiple individual files whose lines are data regarding intersections, errors, or

termination conditions. Given these data, the output was processed in the following manner.

(i) Combine the lines of intersection results from each of the individual files into a single results file (roughly 40-60 MB). (Note that the remaining lines were discarded, but can be otherwise used to analyze the simulations.)

(ii) Filter the results by energies and pitch angles, for example, we only consider energies between 0-52 keV, so anything significantly greater than that range is discarded.

(iii) Compute the translated pitch angle. Although the results returned a final pitch angle, this was the pitch angle of the particle somewhere up or down the magnetic field line from the satellite. Since field lines are equipotentials, the energy remains unchanged, but the pitch angle needs to be adjusted. This adjustment can be made using the magnetic moment, which was conserved throughout the simulation. We begin by computing the magnetic moment using data at the intersection location,

$$\mu = \frac{E \sin^2 \alpha}{\|\mathbf{B}\|} \qquad (4.1)$$

where E is the energy, α is the pitch angle, and $\mathbf{B}$ is the magnetic field vector at the point of boundary intersection.

Given that the magnetic moment is constant along field lines, we can use data at the satellite's physical position to calculate the translated pitch angle by solving for α in equation (4.1),

$$\alpha^* = \arcsin \sqrt{\frac{\mu \|\mathbf{B}^*\|}{E}} \qquad (4.2)$$

where α^* is the translated pitch angle, μ is the previously computed magnetic moment, E is the energy, and $\mathbf{B}^*$ is the magnetic field vector at the satellite's physical position.

Lastly, the translated pitch angle (4.2) must be filtered. Particles navigate up and down field lines until their pitch angle reaches 90 degrees; however, if particles are spawned with a pitch angle of 90 degrees, then they immediately mirror. If said particles were also spawned near the magnetic field minimum, then they will experience a very small range of motion along field lines. As such, it is possible that a particle may not be able to reach a certain position along a field line, or in other words, the position of the satellite. Provided the particle cannot reach the satellite, the formula (4.2)

outputs pitch angles that are complex valued and thus discarded; although there are notably few of these occurrences.

(iv) Given the energy and translated pitch angle of the simulated particle at the intersecting satellite's position, the results must be binned to match that of the observations. Both linear and nearest neighbor binning methods were tried, with negligible differences between the results. Out of convenience for spectrogram reconstruction, the nearest neighbor binning method was chosen.

(v) The two final adjustments to the simulated data are binning the other values, such as position (since the precision of printed results may vary from the true result by some fraction of a meter), and reducing the data to only feature unique results. There were numerous instances where a particle would be detected to contact the magnetic boundary multiple times for an expected single intersection. These repeated hits were typically close and designated to the same bins, meaning that we had multiple, identical predictions. This redundant data was discarded to yield only a final list of data corresponding to unique intersections.

(vi) Provided a list of data for unique intersections from simulation, the next step is to pair up the fluxes from the starting and ending locations to obtain predicted and observed flux values. To do so requires real data from satellite observations for the day. However, the real satellite data includes fill-values such as -1e31, that indicate a failure to record or measure on the satellite's end. If either the starting or ending simulated data had such a flux value, the pair was discarded.

(vii) The final step in post processing was to convert all of the binned values to indices, whereas the predictions and observations are trivially obtained by searching for the indexed value from the 3D flux matrices.

To demonstrate the effect of each step in the process, the percentage of remaining data points are shown in Table (4.1). Note that the initial number of data points is typically in the hundreds of thousands, while the final number of data points is roughly hundreds or thousands.

Table 4.1: Percentage of Total Data Remaining after Each Step

Step	(i)	(ii)	(iii-iv)	(v)	(vi-vii)
Data	100%	98.8%	95.0%	0.55%	0.49%

4.6   Analysis of the Results

In analyzing the results, we have considered and discarded numerous approaches. We have tried a number of Chi-squared-statistics-based metrics; however, the low count regime nullifies the applicability of such statistics. We have contemplated the Cash-statistic (C-statistic) [1] and Poisson statistics, but the lack of a count to flux conversion factor dismisses such methods. Beyond statistical approaches, we designed a binary metric that classifies predictions as successes or failures based off the measured values, but the selection of thresholds (both constant and linear) are all but arbitrary without the count to flux conversion factor, or an approximation of the conversion factor. Although we investigated possible regression fits for the conversion factor as a function of position, energy, and pitch angle; there are additional unclear factors that are necessary to obtain an approximation, for which we cannot currently account. We attempted said binary analysis with thresholds based off of expectations developed from visualizations of the results, but ultimately we decided that the visualizations themselves would be the best method of analyzing the results.

We wanted to observe the change of spectrogram features with respect to the K_p indices. Although we had simulated numerous regions, we concluded that it would be most efficient, especially temporally, to simplify our focus and simulate horizontal and vertical line plots. It follows that we simulated the lines in accordance with Figure (4.5) for all nine combinations of electric and magnetic K_p. The results are then visualized and interpreted separately for each combination.

4.7   Parallel Computing

We initially attempted to optimize the computation of the grid by a straightforward distributive approach; by sending each core an equal combination of radially near and radially distant particles. However, it was determined that the runtime of the particles is not just related to radial position. Analysis revealed that the runtime is a function of position, energy, and pitch angle, none of which are obviously dominant. To overcome this, a simple randomization of the initial particles was employed before distribution across the 120 cores. Once the data had been distributed, the simulations were performed in parallel. Each blade would load the appropriate electric field grid once, which would be accessed by all of the 12 cores which were each simulating a unique particle. Upon finishing a unique particle, the core would progress to the next in the list, until all particles assigned to the blade had been simulated. This process occurred simultaneously

across 10 blades. The success due to the random distribution was decent, with typically a few cores finishing somewhat early and late, and the remaining cores completing their tasks almost simultaneously. This process was repeated nine times for all combinations of a low, medium, and high magnetic and electric K_p. If the user is vigilant, a full simulation (all 4,917 particles for all nine magnetic and electric K_p combinations) can be conducted in little under a week. Simulating everything for a low and medium K_p day could be completed within two weeks.

CHAPTER 5

RESULTS WITH APPLICATION OF REAL DATA

As discussed earlier, one day of consistent low K_p and one day of consistent medium K_p were selected for simulation. For each of these days, nine simulations were executed to cover all nine combinations of low, medium, and high electric and magnetic K_p. Although physically there is only a single K_p, we adjusted the K_p parameter input to the magnetic and electric field models separately to increase the diversity of models.

5.1 Low K_p Day

Provided the resulting data for the nine simulations, we visualize the horizontal and vertical line plots as described. The horizontal line plots are shown on the following page in Figure 5.1, followed by the vertical line plots (Figures 5.3, 5.4, 5.5) on the subsequent pages. These vertical line plots present the simulation results corresponding to the vertical lines depicted in Figure 5.2. Note that all of the horizontal line plots have been combined into a single figure, as they do not indicate a K_p nor offer much information. These will be excluded in the following section.
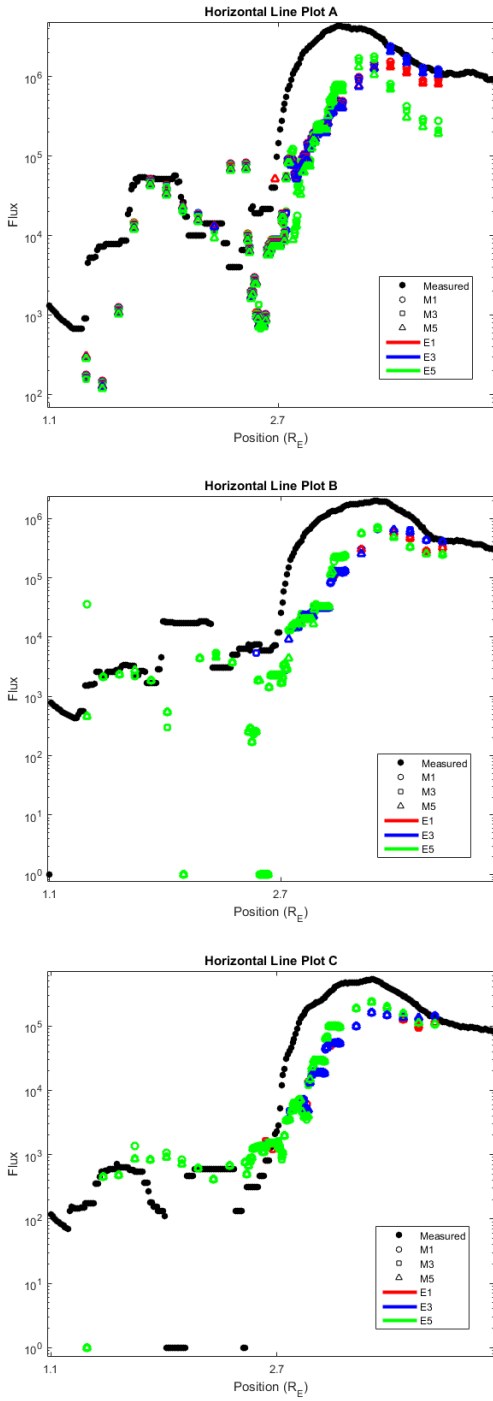
Figure 5.1: Horizontal line plots for the low K_p day. Black is measured, shapes and colors correspond to the input K_p to the magnetic and electric field models, respectively. Note that no particular K_p value stands out.
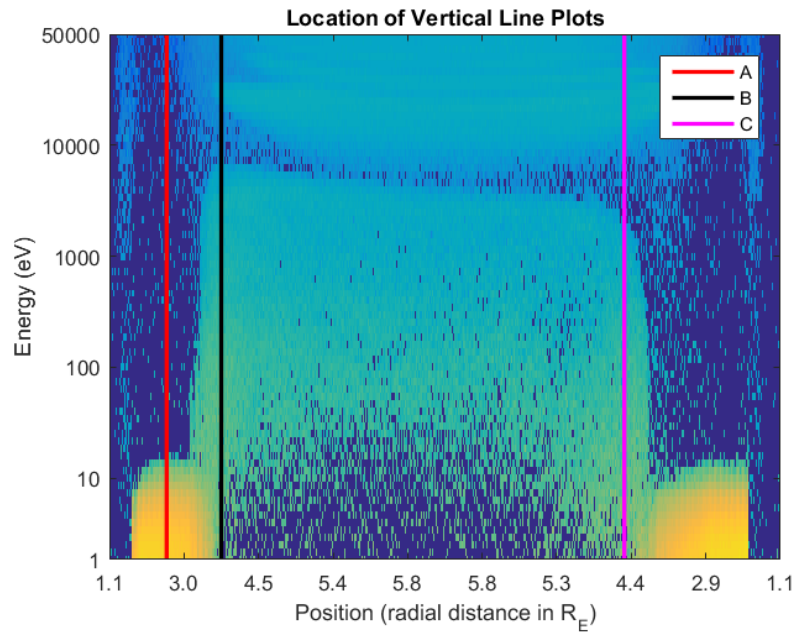
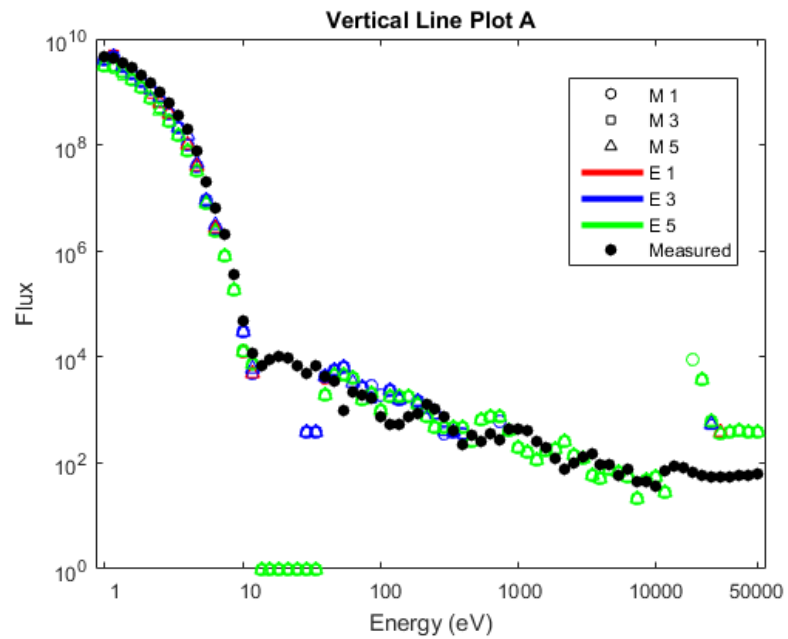Figure 5.2: Location of vertical line plots, low K_p day.

Figure 5.3: Results for vertical line plot A, low K_p day. Black is measured, shapes and colors correspond to the input K_p to the magnetic and electric field models, respectively.
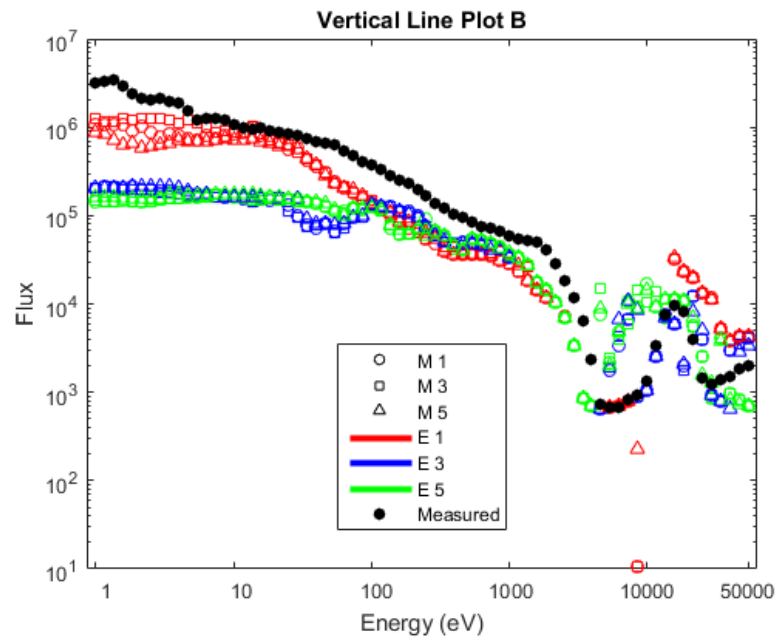
Figure 5.4: Results for vertical line plot B, low K_p day. Black is measured, shapes and colors correspond to the input K_p to the magnetic and electric field models, respectively.
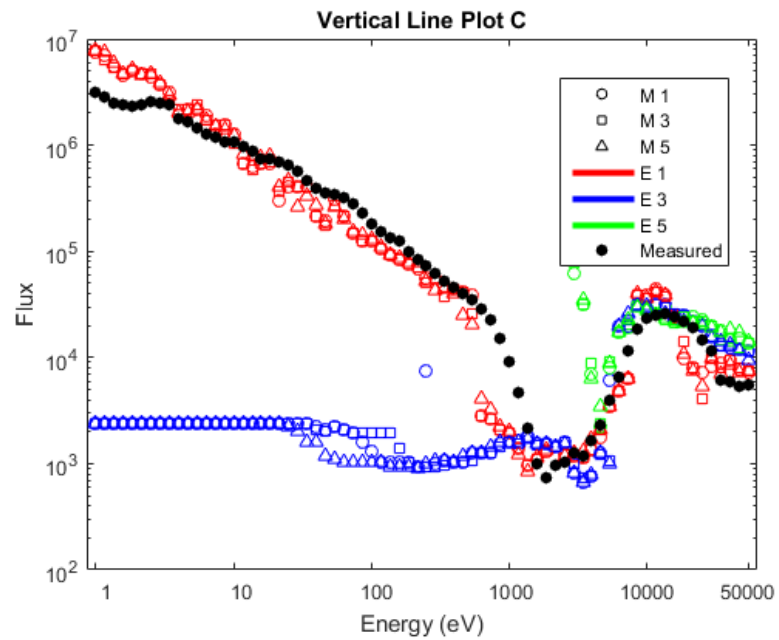

Figure 5.5: Results for vertical line plot C, low K_p day. Black is measured, shapes and colors correspond to the input K_p to the magnetic and electric field models, respectively.

To elaborate on these figures, (5.2) shows the location of the spawns for the vertical line plots, labeling the vertical lines as A, B, and C. Figures (5.3), (5.4), and (5.5) show the resulting predictions of vertical lines A, B, and C, respectively. The colors correspond to the K_p values input to the electric field model: red, blue, and green indicate low, medium, and high K_p, respectively. Similarly, the shapes: circle, square, and triangle correspond to low, medium, and high K_p values, respectively, that were input to the magnetic field model. The black points represent the measured data, observed at the leading satellite. The symbols that most closely match the black points are taken to indicate which input K_p values are the best for this day. Vertical line plot A covers a high-flux region at low energy values, after which it trails off in a region of small fluxes. Vertical line plots B and C traverse through the sides of the flux rectangle centered in the spectrogram, passing through the trough at higher energy, and intersecting the higher-energy denser-flux region at the top of the spectrogram.

5.2 Medium K_p Day

Using the output of the nine simulations for the medium K_p day, we visualize the vertical line plots as described (Figures 5.7, 5.8, 5.9). The locations of these vertical lines are depicted in Figure 5.6. Due to the lack of applicable information in the horizontal line plots (as illustrated earlier), only the vertical line plots are presented below.
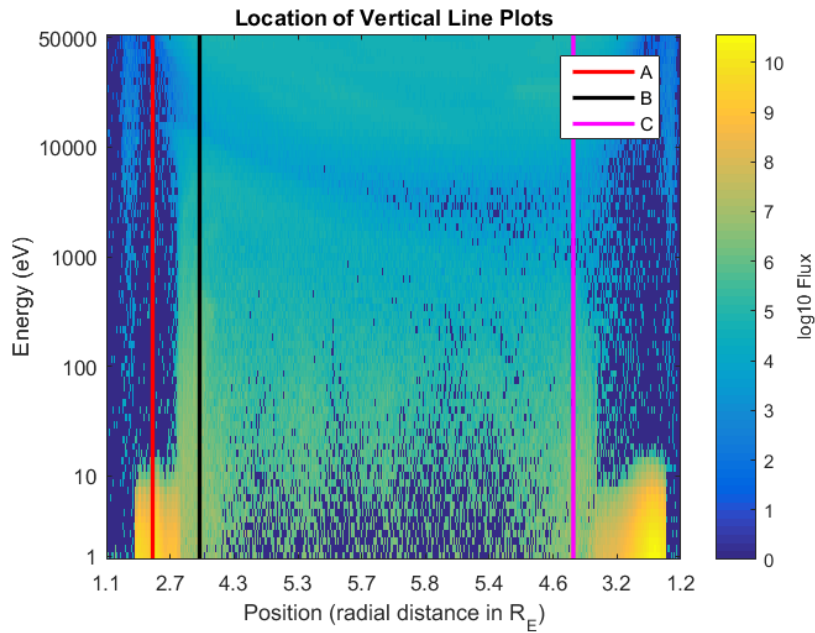
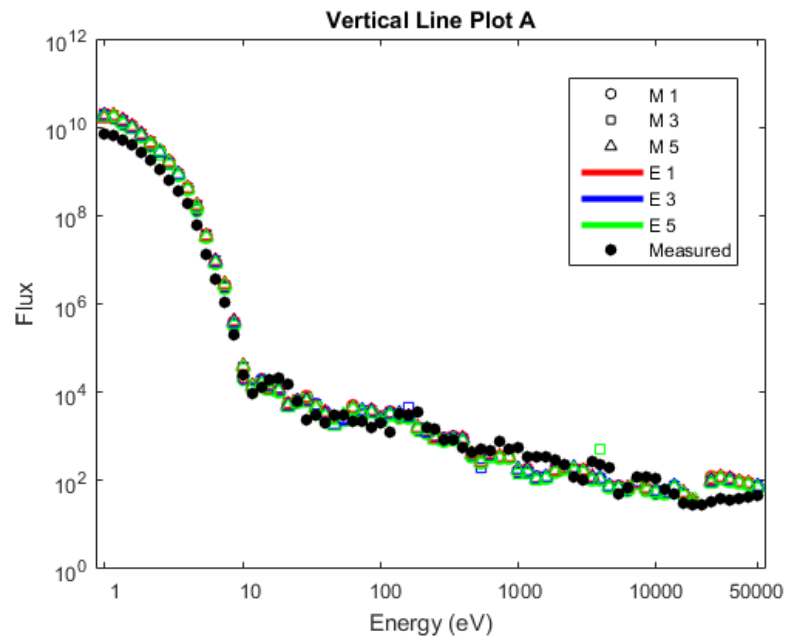Figure 5.6: Location of vertical line plots, medium K_p day.

Figure 5.7: Results for vertical line plot A, medium K_p day. Black is measured, shapes and colors correspond to the input K_p to the magnetic and electric field models, respectively.

Figure 5.8: Results for vertical line plot B, medium K_p day. Black is measured, shapes and colors correspond to the input K_p to the magnetic and electric field models, respectively.

Figure 5.9: Results for vertical line plot C, medium K_p day. Black is measured, shapes and colors correspond to the input K_p to the magnetic and electric field models, respectively.
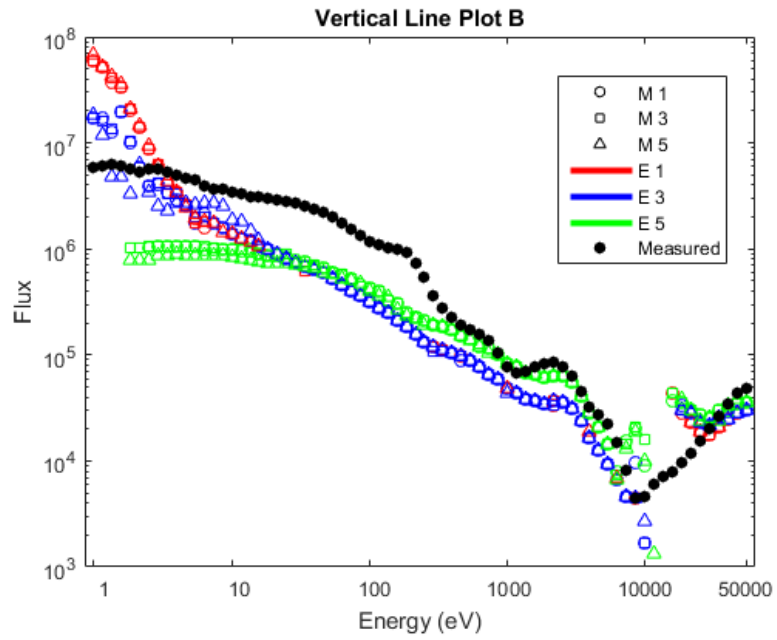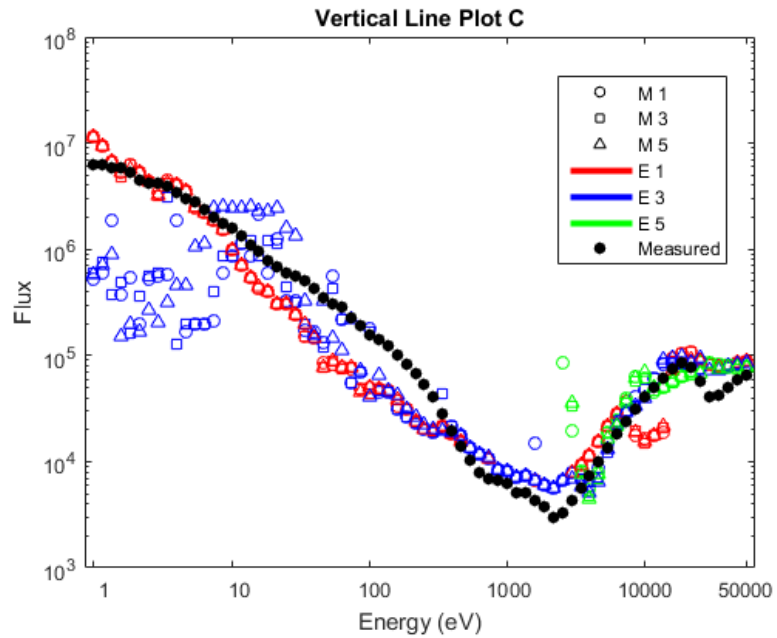
These figures correspond to the second day that has an observed medium K_p value. Figure (5.6) shows the location of the spawns for the vertical line plots, labeling the vertical lines as A, B, and C. Figures (5.7), (5.8), and (5.9) show the resulting predictions of vertical lines A, B, and C, respectively. The colors correspond to the K_p values input to the electric field model: red, blue, and green indicate low, medium, and high K_p, respectively. Similarly, the shapes: circle, square, and triangle correspond to low, medium, and high K_p values, respectively, that were input to the magnetic field model. The black points represent the measured data, observed at the leading satellite. The symbols that most closely match the black points are taken to indicate which input K_p values are the best for this day. Vertical line plot A covers a high-flux region at low energy values, after which it trails off in a region of small fluxes. Vertical line plots B and C traverse through the sides of the flux rectangle centered in the spectrogram, passing through the trough at higher energy, and intersecting the higher-energy denser-flux region at the top of the spectrogram.

CHAPTER 6

DISCUSSION AND CONCLUSIONS

Vertical line plot A for the low K_p day (see Figure 5.3) does not reveal much beyond a consistency in the low flux and high flux regions. That is, the high flux plasmasphere centered around the base of vertical line A (see Figure 5.2) does not change much with respect to electric or magnetic K_p. Similarly, the low flux (near-zero) region of higher energies in the plasmasphere does not change much with respect to K_p either. Note that the fluxes are nonzero in the line plot because we smoothed the spectrograms, but they remain relatively small. For the vertical line plots, a primarily horizontal smoothing kernel was applied.

Vertical line plots B and C for the low K_p day (see Figures 5.4, 5.5) show large differences between the different electric K_p values, with negligible differences with respect to the magnetic K_p. It is clear in both of these vertical line plots that the low electric K_p (red) simulations are far closer to the measured fluxes than the other electric K_p values. This falls off somewhat as energy increases, but this is expected, as the electric field is dominant at lower energies - meaning that the electric K_p should decrease in relevance at higher energies. If we were to determine the K_p from the simulated data without knowledge of the observed K_p, we could easily do so correctly by determining the best matching simulation (visually), then selecting its corresponding electric K_p. However, this is only a conclusion for the low K_p day.

When considering the medium K_p day results, the conclusion is less clear. From vertical line plot A (see Figure 5.7), we see again that the low and high flux regions along the line A (see Figure 5.6) are fairly consistent across varying magnetic and electric K_p values. Given that this result was observed in both the low and medium K_p day, we might conclude that such regions operate independently of the magnetic and electric K_p within the model. However, we are more concerned with the ability to predict the correct K_p by selecting the electric field K_p corresponding to the best matching simulation.

Considering vertical line plot B for the medium K_p day (see Figure 5.8), we notice, if only slightly, that the medium electric field K_p (blue) matches the best. It's closer to the measured fluxes at low energies, then is slightly closer after the

predictions cross over the measured values, until all three of the electric K_p values are under-predicting. To reiterate, the electric field is dominant at low energies, meaning that the left side of these plots (low energies) are more important than the results at high energies, where the high K_p (green) line, for some small energy interval, appears to more closely match the measured fluxes. This seems to weakly push the same conclusion about selecting the electric K_p that corresponds to the best matching simulation; however, let's discuss the third line plot.

In the vertical line plot for C (see Figure 5.9), we notice that the low electric K_p is producing the best matching simulated values early on. Meanwhile, the medium electric K_p model fluxes are rather spread out across nearly two orders of magnitude. Otherwise, there's a section between 10 eV and 100 eV (in energy) where the medium K_p appears to be better than the low electric K_p, but it's not clear which you would conclude; if anything, you might be tempted to conclude the low electric K_p. As a final note regarding this line plot, the predicted flux values were taken from earlier on in the spectrogram; that is, to maintain the assumptions concerning time-stationarity, satellite positioning, and a consistent K_p index, we did not pull values from the satellite orbit beyond what is depicted. Instead, we looped the spectrograms such that any values beyond the orbit were mapped back onto the same orbit (essentially periodic boundary conditions). This is a necessary condition since particles may simulate one full orbit from their spawn location; so particles spawned on the vertical line C (see Figure 5.6) were already roughly 75% through the depicted orbit before they began simulating, and they continue from the front of the spectrogram once they reach the end.

If we attempted to determine the K_p of the medium day without prior knowledge of the observed K_p, the simulation results would lead us to select the best matching simulation values, which is either a K_p of 1 or 3 (low or medium). We would not be able to confidently conclude that we had acquired an estimate of the K_p for the day. Thus, the results of the method are not strong enough to definitively indicate the correct K_p with the current simulations and data; however, this conclusion is subject to change with future investigation.

If we were to continue working on this project, we would pursue a few more options. We would be particularly interested in applying this method to numerous days - perhaps even computing additional vertical line plots (if not the entire spectrograms). We would like to see if the results balanced out over numerous samples to some level of confidence - in our mind there's the possibility that we chose days that were fortunate, and made the result appear better than they should be, or we chose unlucky days, where any other medium K_p day would have more strongly demonstrated the approach in our favor (the consequence of a sample size of 2). Furthermore, it would be interesting to remove some of the assumptions and corresponding constraints placed on the model, namely, time

stationarity. Including time would mean that the magnetic and electric fields are continuously changing. Other than challenges in implementation, time was fixed in the model to avoid the immense computation the time-varying models entail - updating the model coefficients at every time step would increase the run-time many times over (in fact, brief experimentation suggests this could increase run-time by up to 100-fold). Lastly, it would also be intriguing to analyze satellites with greater physical separation, which may lead to the magnetic field model input K_p having a larger effect when a longer particle path is traced. Altogether, any [near] future work would likely face the same constraint we faced throughout the project; computational resources.

REFERENCES

[1] Webster Cash. Parameter estimation in astronomy through application of the likelihood ratio. *The Astrophysical Journal*, 228:939–947, 1979.

[2] Tai L. Chow. *Introduction to electromagnetic theory: a modern perspective*. Jones and Bartlett Learning, 2006.

[3] Richard Fitzpatrick. Lecture notes on magnetic mirrors. University of Texas at Austin. `https://farside.ph.utexas.edu/teaching/plasma/lectures1/node21.html`. March 2011.

[4] Richard Fitzpatrick. Lecture notes on van allen radiation belts. University of Texas at Austin. `https://farside.ph.utexas.edu/teaching/plasma/lectures1/node22.html`. March 2011.

[5] Nicola Fox and James L Burch. *The Van Allen probes mission*. Springer, 2014.

[6] H. O. Funsten. Helium, oxygen, proton, and electron (HOPE) mass spectrometer for the radiation belt storm probes mission. *Space Science Reviews*, 179:1–4, 2013.

[7] Alan C. Hindmarsh, Peter N. Brown, Keith E. Grant, Steven L. Lee, Radu Serban, Dan E. Shumaker, and Carol S. Woodward. SUNDIALS: Suite of nonlinear and differential/algebraic equation solvers. *ACM Transactions on Mathematical Software (TOMS)*, 31(3):363–396, 2005.

[8] Margaret Galland Kivelson and Christopher T Russell. *Introduction to space physics*. Cambridge university press, 1995.

[9] Randall J LeVeque. *Finite difference methods for ordinary and partial differential equations: steady-state and time-dependent problems*. SIAM, 2007.

[10] Yuting Ng, Masahiro Hoshino, Takanobu Amano, Keisuke Shirakawa, and Katsuaki Higashimori. Introduction to motion of charged particles in earth's magnetosphere. Technical report, University of Tokyo, 2013.

[11] Theodore G Northrop. The guiding center approximation to charged particle motion. *Annals of Physics*, 15(1):79 – 101, 1961.

[12] Daniel M Ober, JL Horwitz, and DL Gallagher. Formation of density troughs embedded in the outer plasmasphere by subauroral ion drift events. *Journal of Geophysical Research: Space Physics*, 102(A7):14595–14602, 1997.

[13] Antonius Otto. Lecture notes on single particle dynamics. Geophysical Institute. `http://kfe.fjfi.cvut.cz/~limpouch/plazma/alaska/chap2_particle_motion.pdf`.

[14] John Ashworth Ratcliffe. *An introduction to ionosphere and magnetosphere*. CUP Archive, 1972.

[15] Geoff Reeves. Personal email communication with Geoff Reeves, named contact for the ECT team, 2020.

[16] M. Regi. ULF power fluctuations in the solar-wind parameters and their relationship with the relativistic electron flux at the geosynchronous orbit. *Il Nuovo Cimento*, 39:285–295, 2016.

[17] L. F. Shampine and M. W. Reichelt. The MATLAB ODE suite. *SIAM Journal on Scientific Computing*, 18:1–22, 1997.

[18] Jan Josef Sojka, CE Rasmussen, and Robert W Schunk. An interplanetary magnetic field dependent model of the ionospheric convection electric field. *Journal of Geophysical Research: Space Physics*, 91(A10):11281–11290, 1986.

[19] Harlan Spence and Geoff Reeves. Science operations and data center for rbspect: Data quality and caveats. `https://www.rbsp$-$ect.lanl.gov/science/DataQualityCaveats.php`. 2020.

[20] NOAA SWPC. NOAA space weather scales. `https://www.swpc.noaa.gov/noaa-scales-explanation`, 2020.

[21] Thomas F Tascione. *Introduction to the space environment.* Krieger Publishing Company, 1988.

[22] Erwan Thébault, Christopher C Finlay, Ciarán D Beggan, Patrick Alken, Julien Aubert, Olivier Barrois, Francois Bertrand, Tatiana Bondar, Axel Boness, Laura Brocco, et al. International geomagnetic reference field: the 12th generation. *Earth, Planets and Space*, 67(1):79, 2015.

[23] N. A. Tsyganenko. A magnetospheric magnetic field model with a wrapped tail current sheet. *Planetary and Space Science*, 37:5–20, 1989.

[24] Nikolai A. Tsyganenko. Tsyganenko magnetic field model and GEOPACK s/w, `https://ccmc.gsfc.nasa.gov/modelweb/magnetos/tsygan.html`.

SENSITIVITY OF PARTICLE FLUXES MEASURED BY THE VAN ALLEN PROBES TO VARIATIONS IN THE MODELED MAGNETIC AND ELECTRIC FIELDS

by

John Chilleri

NEW MEXICO TECH
SCIENCE • ENGINEERING • RESEARCH UNIVERSITY